



**IZMIR DEMOCRACY UNIVERSITY**

# **NATURAL & APPLIED SCIENCES JOURNAL**

**IDUNAS**

**E-ISSN: 2645-9000**

**Year: 2023**

**Volume: 6, Issue: 1**



**Table of Contents**

	Sayfa
1. Research Article	1
a. Investigation of The Effect of Adding a Support Sleeve to a Six-Bolt Steel Circular Pipe Connection Clip on Mechanical Properties	
b. Stability of Solution of Quasilinear Parabolic Two-Dimensional with Inverse Coefficient by Fourier Method	9
c. Investigation of the Strength Behavior of a Fuselage Structure Placed In a Linearly Expanding Wing With Circular Ends In Cross-Section	21
d. Cold Pressed Pure Aluminum Powders Sintering With Ultra High Frequency Induction	29
e. Relations of Multiplicative Generalized $(\alpha, \beta)$ – Reverse Derivation and $\alpha$ – Commuting Maps	41

IDUNAS	NATURAL & APPLIED SCIENCES JOURNAL	2023 Vol. 6 No. 1 (1-8)
--------	---------------------------------------	----------------------------------

## Investigation of The Effect of Adding a Support Sleeve to a Six-Bolt Steel Circular Pipe Connection Clip on Mechanical Properties

Research Article

M. Murat Yavuz <sup>1\*</sup> , Osman Berk Buldanhođlu <sup>1</sup> 

<sup>1</sup>İzmir Democracy University, Faculty of Engineering, Mechanical Engineering Department, İzmir.

Author E-mails

[murat.yavuz@idu.edu.tr](mailto:murat.yavuz@idu.edu.tr)

[berkbuldanlioglu@gmail.com](mailto:berkbuldanlioglu@gmail.com)

\*Correspondence to: M. Murat Yavuz, İzmir Democracy University, Faculty of Engineering, Mechanical Engineering Department, İzmir, Turkey.

DOI: 10.38061/idunas.1039978

Received: 22.12.2021; Accepted: 27.12.2022

### Abstract

In this study, the effect of adding a support sleeve for a pipe connection connected with 6 bolts of equivalent spacing was investigated. The research was carried out with a package program that is widely used in finite element analysis. The mouth geometry used for bolts and connection has been simplified for ease of analysis. As a material, steel with standard features was used in the models and static analyses were made. Factors that the connection may encounter most in operating conditions; The axial tension between the pipes, the internal pressure within the pipe and the bending effect with an applied moment were investigated. In addition, pre-loading was applied as displacement to all 6 bolts for axial loading and 3 bolts for bending condition. In the results, the connection region was determined as the region where the stresses were concentrated under all different loading conditions, and it was seen that the applied support sleeve did not show any benefit in reducing the stresses. It was determined that the preload applied to the bolts increased the stresses. Preloading only had a limited positive effect on the bending behavior.

**Keywords:** Pipe connection, Bolt, Stress, Internal pressure.

### 1. INTRODUCTION

Various methods are used to connect pipes to each other. These methods are mostly carried out by means of mechanical and chemical elements. It is necessary to ensure a continuous contact between the connections and to cut off any external contact. This condition, which occurs after the connection is completed, must also be fulfilled if the fluid is transported. It is the most important condition that the fluid does not leak out in the pipe connection. In cases where mechanical and chemical resistance occurs in pipes connected mechanically or chemically and may occur during flow transport, this resistance must be between certain limits. The different methods used for connections in the literature have been researched and the

mechanical problems and efficiency on them are summarized. Most of the failures (Jun et al., 2020) in pipelines with metal parts are corrosion based and the alkalinity of the passing water and the age of the pipe are important factors. Slippage (Tasbihgoo et al., 2004) in mating pipe threads is thought to be the source of noise and fluid leakage. It (Wittenberghe et al., 2011) is recommended that local effects be considered with the entire system for fatigue life investigations in threaded pipe connections. The contact stresses (Shahani and Sharif, 2009) occurring at the connection point of the drill pipe were examined and the highest stresses occurred in the most anterior thread that entered the pipe and in the tooth bed it came into contact with. When the preload effect is applied, the average stress increase is achieved and the stress amplitude is reduced, thereby reducing the effects caused by fatigue. Various mechanical connections (Zaghi and Saaid, 2011) formed in two-way pipe-pin hinges were investigated under earthquake occurrence and it has been observed that the bearing strength of concrete is up to two times higher than the compressive strength of concrete due to boundary effects. Loading capacity (Barsoum and Khalaf, 2015) has been increased by making 3 different pipe-flange designs. A damaged aluminum refrigerant pipe (Stevenson et al., 2017) was examined and found to be broken at the pipe weld. The discontinuous structure (Ren et al., 2018) in the welded joint and the fragile nature of the weld cause a large stress concentration. The effects of seismic effects (Zhao et al., 2022) on the buried gas pipeline under dynamic conditions were investigated and the failures in gaskets and flanges were investigated. In the results of the examination, the use of bolted flange connection is recommended. The pipe failure model (Winkler et al., 2018) that occurs in urban water distribution planning has been investigated and the magnitude of the problems that may occur in distribution has been shown. Leakage investigation (Zhang et al., 2021) was performed on steel wire reinforced polyethylene pipes and it was determined that the over-welded coupling sleeve caused leakage damage. A corroded pipe (Zhang et al., 2020) was repaired using composite material and the axial tensile and internal pressure behavior of the repaired pipe was investigated. Bolted joints were widely used, and preloading is a basic application of bolt connection to prevent the leakage. Bolt preloading (Sawa et al., 2003) was investigated on sealing of pipes at flange connections and the applied axial force was important to ensure the suitable clamping bolt force that was recommended by Pressure Vessel Research Council in USA. The provided connection (Sawa et al., 2006) between preloaded bolt-flange was analyzed for heat and internal pressure effects and connection performance decreased with increasing the temperature. As a result of heat increase on connection, the contact stresses increased. Bolted joints on pipe connections having flanges (Fukuoka and Takaki, 2001) were analyzed for different bolt numbers and stress values were given. Also spiral wound gaskets in bolted-flange connection of pipes (Fukuoka and Takaki, 2003) were analyzed and a uniform preloading values were determined with considering high non-linear stress-strain behavior. If the parameters; pipe diameter and flange thickness (Azim, 2013) were increased, bolt tension increased in the tension of bolts on connection of pipes. Flange thickness-width and diameter of bolt (Tafheem, 2012) have a dominant effect on bolt tension under bending loadings. The preloading was applied with a torque wrench and tightening values of torque wrench (Kondo et al., 2011) was analyzed which included tightening coefficient was given.

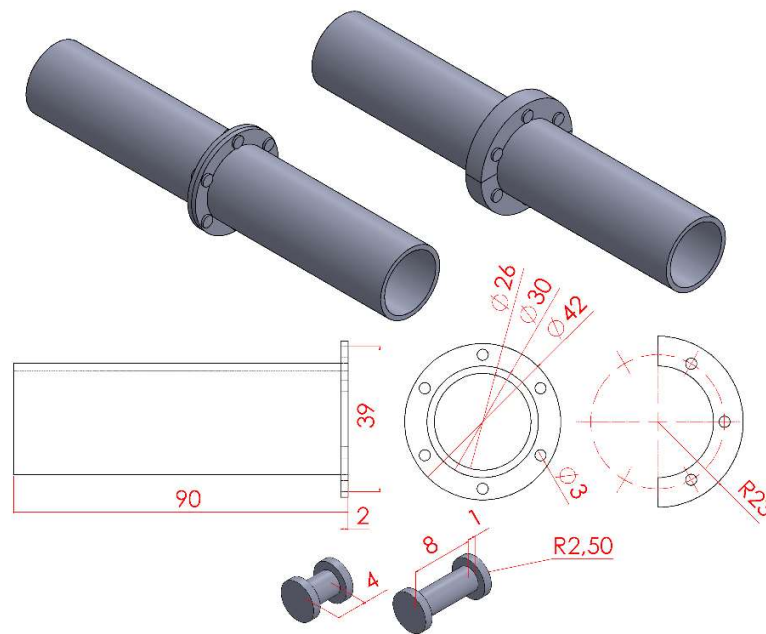
As a result of this study, the effect of the support sleeve that can be used was investigated and its effect on the mechanical properties was examined.

## 2. MATERIAL AND METHOD

Bolt connection is widely preferred in terms of ease of assembly and disassembly. One of the most common problems in these connections is the bending that occurs during the axisymmetric loading on the bolt. Another load that may come from outside to the connection area is the bending condition that commonly occurs in the bolts. In order to reduce bending and external influences, a collar attachment was included and mounted in the connection area using longer bolts. Figure 1 shows two pieces of pipe connected by bolts and their geometrical features. The cuff used is in the form of a flat and simple bracelet, and its

dimensions are shown. Boundary conditions are like each other in case of different loading conditions such as axial tension, internal pressure effect and bending condition. In the case of axial tension, one of the free ends of the pipe is fixed and an axial tensile load of 1000 Pa is applied from the other end. In order to examine the internal pressure effect, the free ends of both necks were fixed, and a pressure of 1000 Pa was applied to the inner surface of the two pipes. To examine the bending condition, the free end of a pipe was fixed, and a pure moment of 120 Nm was applied from the other end. The parts are in full contact, and the contact surface is susceptible to friction. Friction was modelled in accordance with Columb's law of friction and a friction coefficient of 0.3 was determined for the interaction between surfaces. The results are expressed as the Von-Mises stress given in Eq. 1. The modulus of elasticity of the steel material used in the standard specification was determined as 200 GPa and the Poisson ratio was 0.3. All solution results are performed in accordance with elastic boundary conditions.

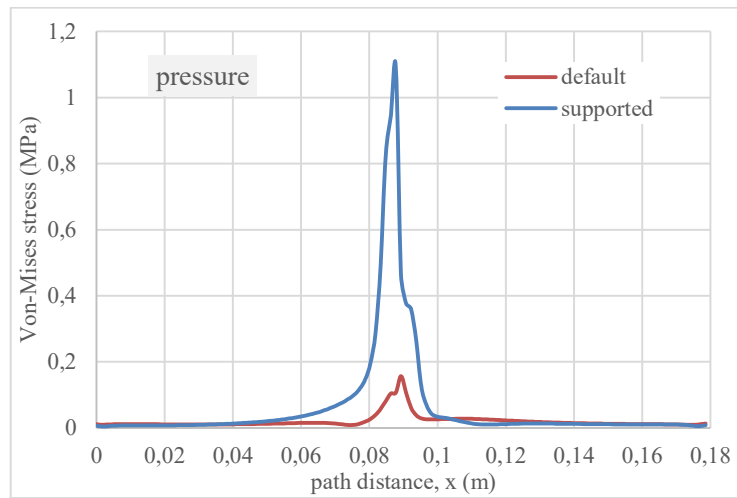
$$\sigma_{VM} = \sqrt{\frac{(\sigma_1 - \sigma_2)^2 + (\sigma_2 - \sigma_3)^2 + (\sigma_3 - \sigma_1)^2}{2}} \tag{1}$$



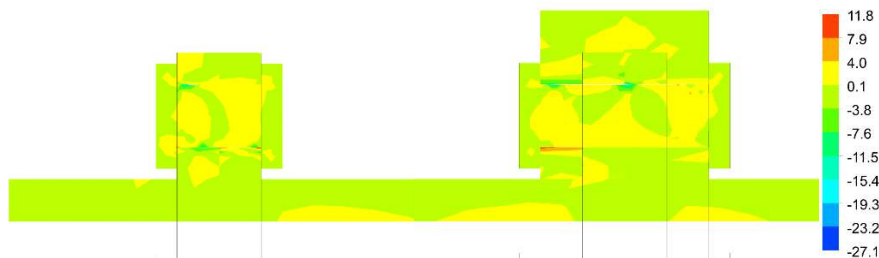
**Figure 1.** The geometry of the pipe joint and the joint support collar.

### 3. RESULTS AND DISCUSSION

In all results, a line contacting the inner surface of the pipes was created and results were obtained by using this line. Fig. 2 shows the stress results for the internally pressurized model. It is seen in the results that the stress is concentrated in the connection region. The applied support sleeve caused the stresses to increase more. Tensile value is approximately 3 times higher.

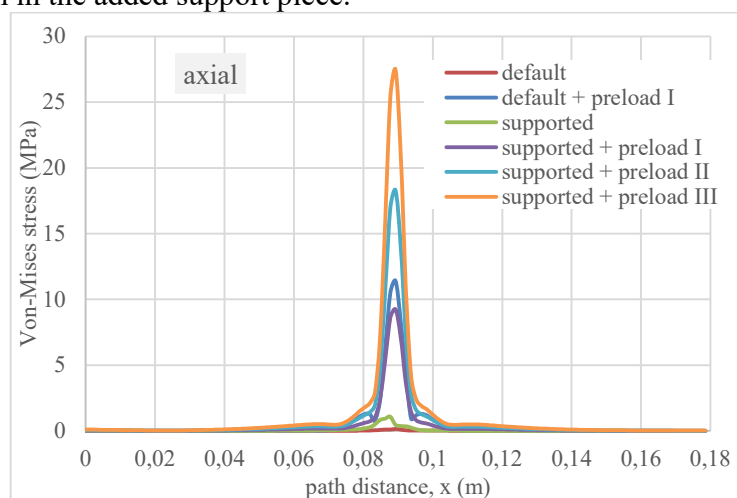


**Figure 2.** Stress distribution on the wall along the pipe direction in the application of in-pipe pressure.

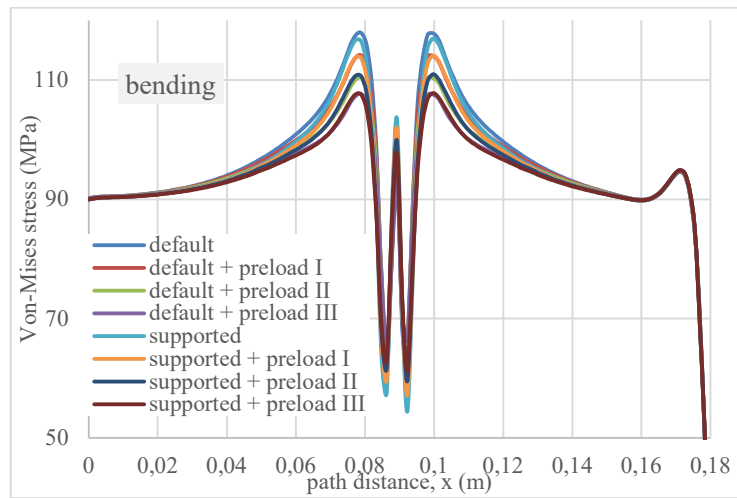


**Figure 3.** Normal stresses occurring in the middle of the pipe in the application of in-pipe pressure.

In Fig. 3, the stress contours formed as a result of the internal pressure are shown for the upper half of the pipes over a plane taken in the middle section. The stresses are given as axial stresses and the values are in the order of MPa. The stresses occurring in the bolt cross section in the normal connection are formed in the form of bending behavior. It is seen that the highest positive stress occurs at the contact corners of the bolt closest to the pipe body. In the support added structure, while stresses of similar values occurred in the bolt structure, the highest normal stress occurred along the entire slot hole length in the socket bed of the support used in contact with the bolt. In the bending state where the bolt size increases, there is more shape change, and this is seen in the added support piece.



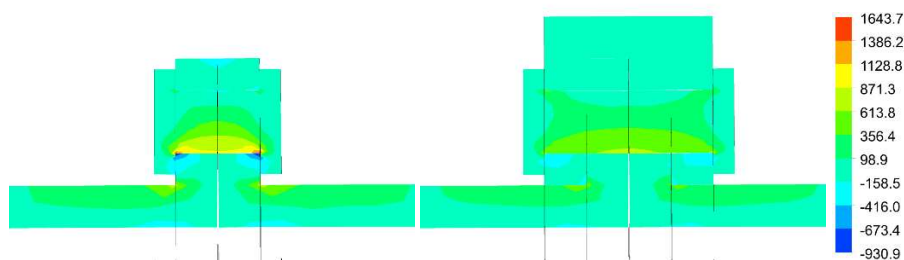
**Figure 4.** Stress distribution in the pipe wall in the axial tension of the pipe end



**Figure 5.** Stress distribution in the pipe wall for bending.

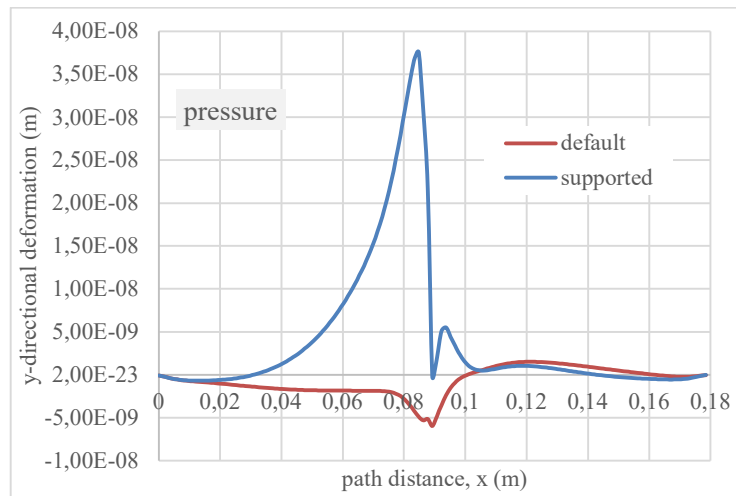
Fig. 4 shows the stress distribution for the axial tension condition. For the case of supported and straight bolt connection, the bolts are also preloaded with displacement condition. The displacements used in preloads I, II and III are 0.01 mm, 0.02 mm, and 0.03 mm. The bolt preload used generally caused the stresses to increase rather than decrease in axial tension. The stresses that occur in the normal bolt connection are lower than the part with the support used. On the other hand, stresses in the reinforced bolt connection for the preload I condition were lower than the normal bolt connection results. There is no region of stress concentration outside the connection region. Stress contours were similarly formed as normal stresses formed as a result of pressure.

Fig. 5 shows the resulting stresses for the bending condition. The preload condition used had an effect for the bending condition and reduced the results to a limited extent. In the results with support pieces, the stress value was less than the results with normal bolt connection. The rightmost side of the graph shows the moment effect applied at the free end and the leftmost side shows the stresses resulting from the support effect. The support stress from  $M \times c / I$  is 90 MPa in the analytical solution and the finite element result in the graph is correct.



**Figure 6.** Normal stresses in the middle of the pipe in bending application (MPa).

Stress contours are shown in Fig. 6. The bending condition exhibited simply supported beam behavior for the pipe section and bolt piece.



**Figure 7.** Deformation distribution on the wall along the pipe direction in the application of in-pipe pressure.

The deformation plot is shown in Fig. 7 for pressure. The support used provided a positive deformation of the inside of the pipe in the outer direction. For the normal connection situation, it is seen that the pipe corners are bent locally towards the inside of the pipe at the junction. The deformation is higher in the supported connection.

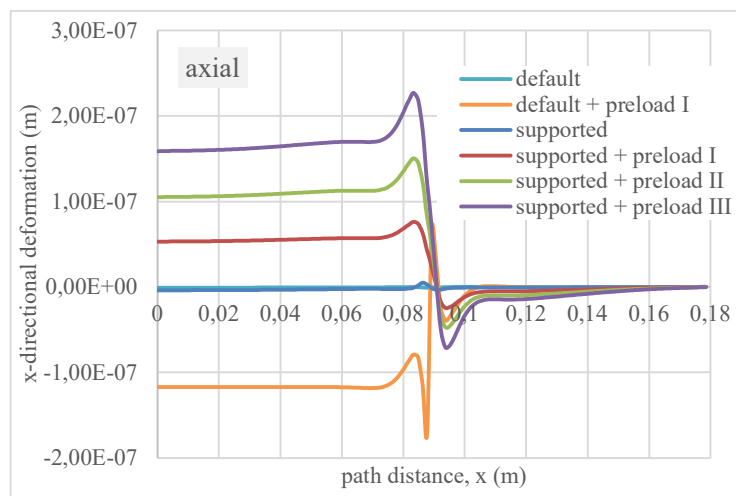


**Figure 8.** Deformation distribution in the wall along the pipe direction in axial drawing application

The deformation results for the axial tensile condition are shown in Fig. 8. It is seen that the deformation is more in the supported part. It was observed that the applied preload did not reduce the deformation. However, the axial deformation in the supported joint occurred positively. It is a negative effect for fluid leakage. This situation occurred in the negative direction for the normal bolt connection.



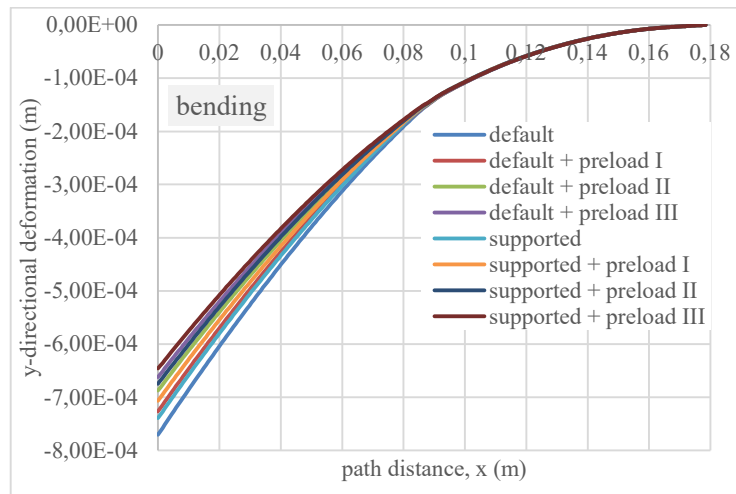


**Figure 9.** Deformation distribution on the wall along the pipe direction in bending application.

In Fig. 9, the deformation in the vertical direction is shown for the bending condition. Although the deformation results in the pipe section where the support is located after 0.9 m are similar, the bending situation seems to be dominant at the point where the 0-0.09-meter moment is applied. The highest deformation occurred in the normal connection condition. The applied preload reduced the deformation. The preload on the bolts was applied only for the 3 bolts in the upper part.

#### 4. CONCLUSION

In this study, normal bolts and bolt connection with support ring were applied in connecting the pipes and their structural behavior was investigated under 3 different mechanical conditions. In general, the following findings were obtained in the results of the pre-loading of the bolts;

- In all different loading conditions, the joint zone is determined as the zone of concentration of stresses.
- The applied support sleeve caused the stresses to increase up to 3 times.
- Larger shape changes occurred in the bolts in the support sleeve used.
- The preloads applied to the bolts caused the stresses to increase in the axial tension condition.
- Preloads applied in case of axial tension caused mostly positive deformation of the joint and are negative for fluid leakage.

#### 5. REFERENCES

1. Jun, J. H., Park, J. K., Bae, C. H. (2020). Factors affecting steel water-transmission pipe failure and pipe-failure mechanisms. *Journal of Environmental Engineering*, 146(6), 04020034.
2. Tasbihgoo, F., Caffrey, J. P., Masri, S. F. (2004). Nonlinear finite element analysis of a threaded pipe connection. *ASME/JSME 2004 Pressure Vessels and Piping Conference*, 173-179.
3. Wittenberghe, J. V., Baets, P. D., Waele, W. D., Galle, T., Bui, T. T., Roeck, G. D. (2011). Design characteristics that improve the fatigue life of threaded pipe connections. *Sustainable Construction and Design*, 2(2), 334-341.
4. Shahani, A. R., Sharif, S. M. H. (2009). Contact stress analysis and calculation of stress concentration factors at the tool joint of a drill pipe. *Materials and Design*, 30, 3615–3621.
5. Zaghi, A. E., Saiid, S. M. (2011). Bearing and shear failure of pipe-pin hinges subjected to earthquakes. *American Society of Civil Engineers*, 16(3), 340-350

6. Barsoum, I., Khalaf, A.M. (2015). Evaluation of a pipe-flange connection replacing fusion welding. *Procedia Engineering*, 130, 446-452.
7. Stevenson, M. E., Iwand, H. C., McDougall, J. L., Umberger, P. D., Wilkinson, J. A., Kenner, M. T., Stone, D. H. (2017). Failure analysis of an aluminum chiller pipe by experimental simulation and stress analysis. *J Fail. Anal. and Preven.*, 17, 1090–1098.
8. Ren, F., Li, B., Tang, X. (2018). Failure analysis of collecting pipe head used in ammonia refrigerating system. *IOP Conf. Series: Materials Science and Engineering*, 382, 022101.
9. Zhao, K., Jiang, N., Zhou, C., Li, H., Cai, Z., Zhu, B. (2022). Dynamic behavior and failure of buried gas pipeline considering the pipe connection form subjected to blasting seismic waves. *Thin-Walled Structures*, 170, 108495.
10. Winkler, D., Haltmeier, M., Kleidorfer, M., Rauch, W., Tscheikner-Gratl, F. (2018). Pipe failure modelling for water distribution networks using boosted decision trees. *Structure and Infrastructure Engineering*, 14(10), 1402-1411.
11. Zhang, X., Hou, L., Li, H., Qi, G., Qi, D. (2021). Leakage analysis of steel wire reinforced polyethylene composite pipe used for wastewater transportation. *Engineering Failure Analysis*, 130, 105750.
12. Zhang, Y., Cheng, Z., Jia, Z. (2020). Failure loads analysis of corroded pipe repaired by composite material under tension and internal pressure. *Journal of Marine Engineering & Technology*.doi: 10.1080/20464177.2020.1826675.
13. Sawa, T., Matsumoto, M., Nagata, S. (2003). Effects of scatter in bolt preload of pipe flange connections with gaskets on sealing performance. *ASME Pressure Vessels and Piping Conference*, 20-24 July 2003, Cleveland, Ohio, USA.
14. Sawa, T., Takagi, Y., Yamada, K. (2006). Evaluation of the sealing performance in bolted flange connection under heat condition and internal pressure (the effect of scatter in bolt preloads). *ASME Pressure Vessels and Piping Division Conference*, July 23-27, 2006, Vancouver, BC, Canada.
15. Fukuoka, T., Takaki, T. (2001). Finite element simulation of bolt-up process of pipe flange connections. *Journal of Pressure Vessel Technology*, *Transactions of the ASME*, 282- 287.
16. Fukuoka, T., Takaki, T. (2003). Finite element simulation of bolt-up process of pipe flange connections with spiral wound gasket. *Journal of Pressure Vessel Technology*, *Transactions of the ASME*, November 2003, 371-378.
17. Azim, R. (2013). An analytical investigation on bolt tension of a flanged steel pipe joint subjected to bending moments. *International Journal of Engineering and Applied Sciences*, 2(3), 71-81.
18. Tafheem, Z. (2012). Investigation on bolt tension of flanged pipe joint subjected to bending. *Master of Science in Civil Engineering*, Bangladesh University of Engineering and Technology, February 2012.
19. Kondo, K., Omiya, Y., Kobayashi, T., Sawa, T. (2011). Scatter of bolt preloads in pipe flange connection tightened by impact wrench and the effect on sealing performance. *ASME International Mechanical Engineering Congress and Exposition*, November 11–17, 2011 Denver, Colorado, USA.

IDUNAS	NATURAL & APPLIED SCIENCES JOURNAL	2023 Vol. 6 No. 1 (9-20)
--------	---------------------------------------	-----------------------------------

## Stability of Solution of Quasilinear Parabolic Two-Dimensional with Inverse Coefficient by Fourier Method

İrem Bağlan\*<sup>1</sup> 

<sup>1</sup>Department of Mathematics, Kocaeli University, Kocaeli, Turkey.

Author E-mails  
isakinc@kocaeli.edu.tr

\*Correspondence to: İrem Bağlan, Department of Mathematics, Kocaeli University, Kocaeli, Turkey.

DOI: 10.38061/idunas.1296023

Received:11.05.2023; Accepted: 19.06.2023

### Abstract

In this article, the heat inverse two-dimensional quasilinear parabolic problem is examined. The stability and numerical solution for the problem are discussed. Since the problem is not linear, Picard's successive approximations theorem is used. In the numerical part, the solution is made with the finite difference and linearization method.

**Keywords:** Inverse problem, Fourier method, Periodic boundary conditions, Picard Method, Two-dimension parabolic problem, Fourier coefficient.

### 1. INTRODUCTION

Inverse problems are used to find an unknown character of a matter or a place. Especially inverse problems are important for many calculations used in aircraft, missiles and submarines. In geophysics, the inverse problem is finding subsurface inhomogeneities. When measuring the frequencies of a material, the inverse problem is finding whether there is a defect (a hole in a metal) in that material. There may be a tumor or some abnormalities in the human body in medicine. The inverse problem is examined [4], [5],[6]. It is used in many fields such as population, electrochemistry, engineering, chemistry. The problems with nonlocal boundary conditions discussed in this article are not easy to study. Various boundary conditions have been studied in this area [1],[2],[3].

### 2. MATERIAL AND METHODS

For the solution of this problem, the Fourier Method and Picard successive approximations method were used, while the linearization method was used for the numeric solution. It was used implicit finite-difference method for numeric problem.

**3. STABILITY OF SOLUTIONS**

$$\frac{\partial v}{\partial t} = b(t) \frac{\partial^2 v}{\partial x^2} + \frac{\partial^2 v}{\partial y^2} + h(\alpha, \beta, \tau, v), \tag{1}$$

$$v(\alpha, \beta, 0) = \varphi(\alpha, \beta), \alpha \in [0, \pi], \beta \in [0, \pi] \tag{2}$$

$$\begin{aligned} v(0, \beta, \tau) &= v(\pi, \beta, \tau), \beta \in [0, \pi], \tau \in [0, T] \\ v(\alpha, 0, \tau) &= v(\alpha, \pi, \tau), \alpha \in [0, \pi], \tau \in [0, T] \\ v_\alpha(0, \beta, \tau) &= v_\alpha(\pi, \beta, \tau), \beta \in [0, \pi], \tau \in [0, T] \\ v_\beta(\alpha, 0, \tau) &= v_\beta(\alpha, \pi, \tau), \alpha \in [0, \pi], \tau \in [0, T] \end{aligned} \tag{3}$$

$$k(t) = \int_0^\pi \int_0^\pi \alpha \beta v(\alpha, \beta, \tau) d\alpha d\beta, \tau \in [0, T], \tag{4}$$

where (1) is the inverse coefficient problem, (2) is the initial condition, (3) are the periodic boundary conditions [8] and (4) is the integral overdetermination data ( $k(t)$  is heat diffusions) [7].

As known, in Fourier Method, we get the following structure:

$$\begin{aligned} v(\alpha, \beta, \tau) &= \frac{v_0(\tau)}{4} \\ &+ \sum_{m,n=1}^{\infty} v_{scmn}(\tau) \sin(2m\alpha) \cos(2n\beta) \\ &+ \sum_{m,n=1}^{\infty} v_{smn}(\tau) \sin(2m\alpha) \sin(2n\beta). \\ v_0(\tau) &= v_0(0) + \frac{4}{\pi^2} \int_0^\tau \int_0^\pi \int_0^\pi h(\alpha, \beta, \tau, v) d\alpha d\beta d\tau \\ &\quad - \int_0^\tau [b(r)(2m)^2 + (2n)^2] dr \\ v_{cmn}(\tau) &= v_{cmn}(0) e^{-\int_0^\tau [b(s)(2m)^2 + (2n)^2] ds} \\ &+ \frac{4}{\pi^2} \int_0^\tau \int_0^\pi \int_0^\pi e^{-\int_0^\tau [b(r)(2m)^2 + (2n)^2] dr} h(\alpha, \beta, \tau, v) \cos(2m\alpha) \cos(2n\beta) d\alpha d\beta d\tau \\ v_{csmn}(\tau) &= v_{csmn}(0) e^{-\int_0^\tau [b(r)(2m)^2 + (2n)^2] dr} \\ &+ \frac{4}{\pi^2} \int_0^\tau \int_0^\pi \int_0^\pi e^{-\int_0^\tau [b(r)(2m)^2 + (2n)^2] dr} h(\alpha, \beta, \tau, v) \cos(2m\alpha) \sin(2n\beta) d\alpha d\beta d\tau \end{aligned}$$

$$v_{scmn}(\tau) = v_{scmn}(0)e^{-\int_0^\tau [b(r)(2m)^2 + (2n)^2] dr} + \frac{4}{\pi^2} \int_0^\tau \int_0^\pi \int_0^\pi e^{-\int_0^\tau [b(r)(2m)^2 + (2n)^2] dr} h(\alpha, \beta, \tau, v) \sin(2m\alpha) \cos(2n\beta) d\alpha d\beta d\tau$$

$$v_{smn}(\tau) = v_{smn}(0)e^{-\int_0^\tau [b(r)(2m)^2 + (2n)^2] dr} + \frac{4}{\pi^2} \int_0^\tau \int_0^\pi \int_0^\pi e^{-\int_0^\tau [b(r)(2m)^2 + (2n)^2] dr} h(\alpha, \beta, \tau, v) \sin(2m\alpha) \sin(2n\beta) d\alpha d\beta d\tau$$

Then we obtain the solution:

$$v(\alpha, \beta, \tau) = \frac{1}{4} \left( \varphi_0 + \frac{4}{\pi^2} \int_0^\tau h_0(\tau, v) d\tau \right) + \sum_{m,n=1}^{\infty} \left( \varphi_{cmn} + \frac{4}{\pi^2} \int_0^\tau e^{-\int_0^\tau [b(r)(2m)^2 + (2n)^2] dr} h_{cmn}(\tau, v) d\tau \right) \cos(2m\alpha) \cos(2n\beta) + \sum_{m,n=1}^{\infty} \left( \varphi_{csmn} + \frac{4}{\pi^2} \int_0^\tau e^{-\int_0^\tau [b(r)(2m)^2 + (2n)^2] dr} h_{csmn}(\tau, v) d\tau \right) \cos(2m\alpha) \sin(2n\beta) + \sum_{m,n=1}^{\infty} \left( \varphi_{scmn} + \frac{4}{\pi^2} \int_0^\tau e^{-\int_0^\tau [b(r)(2m)^2 + (2n)^2] dr} h_{scmn}(\tau, v) d\tau \right) \sin(2m\alpha) \cos(2n\beta) + \sum_{m,n=1}^{\infty} \left( \varphi_{smn} + \frac{4}{\pi^2} \int_0^\tau e^{-\int_0^\tau [b(r)(2m)^2 + (2n)^2] dr} h_{smn}(\tau, v) d\tau \right) \sin(2m\alpha) \sin(2n\beta)$$

Here,

$$\varphi_0 = v_0(0),$$

$$\varphi_{cmm} = v_{cmm}(0)e^{-\int_0^t [b(r)(2m)^2 + (2n)^2] dr},$$

$$\varphi_{csmm} = v_{csmm}(0)e^{-\int_0^t [b(r)(2m)^2 + (2n)^2] dr},$$

$$\varphi_{scmm} = v_{scmm}(0)e^{-\int_0^t [b(r)(2m)^2 + (2n)^2] dr},$$

$$\varphi_{smm} = v_{smm}(0)e^{-\int_0^t [b(r)(2m)^2 + (2n)^2] dr}.$$

Let's assume the following rules for the functions used in the problem:

(A1)  $k(t) \in C^1[0, T]$

(A2)  $\varphi(\alpha, \beta) \in C^{1,1}([0, \pi] \times [0, \pi])$ ,  
 $\varphi(0, \beta) = \varphi(\pi, \beta), \varphi_x(0, \beta) = \varphi_x(\pi, \beta), \int_0^\pi \int_0^\pi \alpha\beta\varphi(\alpha, \beta) d\alpha d\beta = k(0)$ ,  
 $\varphi(\alpha, 0) = \varphi(\alpha, \pi), \varphi_y(\alpha, 0) = \varphi_y(\alpha, \pi)$ ,

(A3) Let  $h(\alpha, \beta, \tau, v)$  have the following properties:

$$\left| \frac{\partial h(\alpha, \beta, \tau, v)}{\partial \alpha} - \frac{\partial h(\alpha, \beta, \tau, \bar{v})}{\partial \alpha} \right| \leq l(\alpha, \beta, \tau) |v - \bar{v}|,$$

$$\left| \frac{\partial h(\alpha, \beta, \tau, v)}{\partial \beta} - \frac{\partial h(\alpha, \beta, \tau, \bar{v})}{\partial \beta} \right| \leq l(\alpha, \beta, \tau) |v - \bar{v}|,$$

$$\left| \frac{\partial h(\alpha, \beta, \tau, v)}{\partial \alpha \partial \beta} - \frac{\partial h(\alpha, \beta, \tau, \bar{v})}{\partial \alpha \partial \beta} \right| \leq l(\alpha, \beta, \tau) |v - \bar{v}|, \text{ where } l(\alpha, \beta, \tau) \in L_2(D), l(\alpha, \beta, \tau) \geq 0,$$

(2)  $h(\alpha, \beta, \tau, v) \in C^{2,2,0}[0, \pi], \tau \in [0, T]$ ,

(3)  $h(\alpha, \beta, \tau, v)|_{\alpha=0} = h(\alpha, \beta, \tau, v)|_{\alpha=\pi}$ ,

$h_\alpha(\alpha, \beta, \tau, v)|_{\alpha=0} = h_\alpha(\alpha, \beta, \tau, v)|_{\alpha=\pi}$ ,

$h_\beta(\alpha, \beta, \tau, v)|_{\beta=0} = h_\beta(\alpha, \beta, \tau, v)|_{\beta=\pi}$ ,

$h_{\alpha\beta}(\alpha, \beta, \tau, v)|_{\alpha=0} = h_{\alpha\beta}(\alpha, \beta, \tau, v)|_{\alpha=\pi}$ ,

$h_{\alpha\beta}(\alpha, \beta, \tau, v)|_{\beta=0} = h_{\alpha\beta}(\alpha, \beta, \tau, v)|_{\beta=\pi}$ .

$$\int_0^\pi \int_0^\pi \alpha\beta v_t(\alpha, \beta, \tau) d\alpha d\beta = k'(\tau), 0 \leq t \leq T.$$

$$b(\tau) = \frac{k'(\tau) - \int_0^\pi \int_0^\pi xyh(\alpha, \beta, \tau, v) d\alpha d\beta - \frac{\pi^3}{2} v_\beta(\pi, \tau)}{\frac{\pi^3}{2} v_\alpha(\pi, \tau)}.$$

**Definition 1.**

Show the set  $\{v(\tau)\} = \{v_0(\tau), v_{c_{mn}}(\tau), v_{c_{smn}}(\tau), v_{s_{mn}}(\tau), v_{s_{mn}}(\tau)\}$  of continuous functions on  $[0, T]$  which satisfy the condition.

$$\max_{0 \leq t \leq T} \frac{|v_0(\tau)|}{4} + \sum_{m,n=1}^{\infty} \left( \max_{0 \leq t \leq T} |v_{c_{mn}}(\tau)| + \max_{0 \leq t \leq T} |v_{c_{smn}}(\tau)| + \max_{0 \leq t \leq T} |v_{s_{mn}}(\tau)| + \max_{0 \leq t \leq T} |v_{s_{mn}}(\tau)| \right) < \infty .$$

$$\|v(\tau)\| = \max_{0 \leq t \leq T} \frac{|v_0(\tau)|}{4} + \sum_{m,n=1}^{\infty} \left( \max_{0 \leq t \leq T} |v_{c_{mn}}(\tau)| + \max_{0 \leq t \leq T} |v_{c_{smn}}(\tau)| + \max_{0 \leq t \leq T} |v_{s_{mn}}(\tau)| + \max_{0 \leq t \leq T} |v_{s_{mn}}(\tau)| \right)$$

is called Banach norm.

**Theorem 1:** According to (A1)-(A3), the solution of (1)-(4) is constantly dependent on the data.

**Proof:**

Let  $\theta = \{\varphi, k, h\}, \bar{\theta} = \{\bar{\varphi}, \bar{k}, \bar{h}\}$  and  $M, L_i, i = 1, 2$  positive constant.

$$\|h\|_{C^{1,1,0}[\Gamma]} \leq M, \|\bar{h}\|_{C^{1,1,0}[\Gamma]} \leq M,$$

$$\|\varphi\|_{C^3[0,\pi]} \leq L_1, \|\bar{\varphi}\|_{C^3[0,\pi]} \leq L_1,$$

$$\|k\|_{C^1[0,T]} \leq L_2, \|\bar{k}\|_{C^1[0,T]} \leq L_2,$$

$$\|\theta\| = (\|k\|_{C^1[0,T]} + \|\varphi\|_{C^{1,1}[0,\pi]} + \|h\|_{C^{1,1,0}[\Gamma]}).$$

$$v - \bar{v} = \frac{(\varphi_0 - \bar{\varphi}_0)}{4} - \int_0^t [b(r)(2m)^2 + (2n)^2] dr \sum_{m,n=1}^{\infty} \varphi_{c_{mn}} e^{-\tau} \cos(2m\alpha) \cos(2n\beta)$$

$$\sum_{m,n=1}^{\infty} \frac{\bar{\varphi}_{c_{mn}}}{\tau} - \int_0^t [\bar{b}(r)(2m)^2 + (2n)^2] dr \cos(2m\alpha) \cos(2n\beta)$$

$$+ \sum_{m,n=1}^{\infty} \varphi_{c_{smn}} e^{-\tau} - \int_0^t [b(r)(2m)^2 + (2n)^2] dr \cos(2m\alpha) \sin(2n\beta)$$

$$\begin{aligned}
 & + \sum_{m,n=1}^{\infty} \frac{\varphi_{csmn}}{e^{\tau}} \int_0^t \left[ \bar{b}(r)(2m)^2 + (2n)^2 \right] dr \cos(2m\alpha) \sin(2n\beta) \\
 & + \sum_{m,n=1}^{\infty} \varphi_{scmn} e^{-\int_0^t [b(r)(2m)^2 + (2n)^2] dr} \sin(2m\alpha) \cos(2n\beta) \\
 & + \sum_{m,n=1}^{\infty} \frac{\varphi_{scmn}}{e^{\tau}} \int_0^t \left[ \bar{b}(r)(2m)^2 + (2n)^2 \right] dr \sin(2m\alpha) \cos(2n\beta) \\
 & + \sum_{m,n=1}^{\infty} \varphi_{smn} e^{-\int_0^t [b(r)(2m)^2 + (2n)^2] dr} \sin(2m\alpha) \sin(2n\beta) \\
 & + \sum_{m,n=1}^{\infty} \frac{\varphi_{smn}}{e^{\tau}} \int_0^t \left[ \bar{b}(r)(2m)^2 + (2n)^2 \right] dr \sin(2m\alpha) \sin(2n\beta) \\
 & + \frac{1}{4} \left( \begin{aligned} & \frac{4}{\pi^2} \int_0^t \int_0^{\pi} \int_0^{\pi} [h(\alpha, \beta, \tau, v) - h(\alpha, \beta, \tau, \bar{v})] \\ & e^{-\int_0^t [\bar{b}(r)(2m)^2 + (2n)^2] dr} d\alpha d\beta d\tau \end{aligned} \right) \\
 & + \frac{1}{4} \left( \begin{aligned} & \frac{4}{\pi^2} \int_0^t \int_0^{\pi} \int_0^{\pi} h(\alpha, \beta, \tau, \bar{v}) \\ & e^{-\int_0^t [b(r)(2m)^2 + (2n)^2] dr} - e^{-\int_0^t [\bar{b}(r)(2m)^2 + (2n)^2] dr} \\ & d\alpha d\beta d\tau \end{aligned} \right) \\
 & + \sum_{m,n=1}^{\infty} \frac{4}{\pi^2} \int_0^t \int_0^{\pi} \int_0^{\pi} [h(\alpha, \beta, \tau, v) - h(\alpha, \beta, \tau, \bar{v})] \\
 & e^{-\int_0^t [\bar{b}(r)(2m)^2 + (2n)^2] dr} \cos(2m\alpha) \cos(2n\beta) d\alpha d\beta d\tau
 \end{aligned}$$



$$\begin{aligned}
 & + \sum_{k=1}^{\infty} \frac{4}{\pi^2} \int_0^t \int_0^{\pi} \int_0^{\pi} h(\alpha, \beta, \tau, \bar{v}) \\
 & \left( \begin{array}{cc} -\int_0^t [b(r)(2m)^2 + (2n)^2] dr & -\int_0^t [\bar{b}(r)(2m)^2 + (2n)^2] dr \\ e^{\tau} & -e^{\tau} \end{array} \right) \\
 & \cos(2m\alpha) \cos(2n\beta) d\alpha d\beta d\tau \\
 & + \sum_{m,n=1}^{\infty} \frac{4}{\pi^2} \int_0^t \int_0^{\pi} \int_0^{\pi} [h(\alpha, \beta, \tau, v) - h(\alpha, \beta, \tau, \bar{v})] \\
 & - \int_0^t [\bar{b}(r)(2m)^2 + (2n)^2] dr \\
 & e^{\tau} \cos(2m\alpha) \sin(2n\beta) d\alpha d\beta d\tau \\
 & + \sum_{m,n=1}^{\infty} \frac{4}{\pi^2} \int_0^t \int_0^{\pi} \int_0^{\pi} h(\alpha, \beta, \tau, \bar{v}) \\
 & \left( \begin{array}{cc} -\int_0^t [b(r)(2m)^2 + (2n)^2] dr & -\int_0^t [\bar{b}(r)(2m)^2 + (2n)^2] dr \\ e^{\tau} & -e^{\tau} \end{array} \right) \\
 & \cos(2m\alpha) \sin(2n\beta) d\alpha d\beta d\tau \\
 & + \sum_{m,n=1}^{\infty} \frac{4}{\pi^2} \int_0^t \int_0^{\pi} \int_0^{\pi} [h(\alpha, \beta, \tau, v) - h(\alpha, \beta, \tau, \bar{v})] \\
 & - \int_0^t [\bar{b}(r)(2m)^2 + (2n)^2] dr \\
 & e^{\tau} \sin(2m\alpha) \cos(2n\beta) d\alpha d\beta d\tau \\
 & + \sum_{m,n=1}^{\infty} \frac{4}{\pi^2} \int_0^t \int_0^{\pi} \int_0^{\pi} h(\alpha, \beta, \tau, \bar{v}) \\
 & \left( \begin{array}{cc} -\int_0^t [b(r)(2m)^2 + (2n)^2] dr & -\int_0^t [\bar{b}(r)(2m)^2 + (2n)^2] dr \\ e^{\tau} & -e^{\tau} \end{array} \right) \\
 & \sin(2m\alpha) \cos(2n\beta) d\alpha d\beta d\tau
 \end{aligned}$$

$$\begin{aligned}
 & + \sum_{m,n=1}^{\infty} \frac{4}{\pi^2} \int_0^t \int_0^{\pi} \int_0^{\pi} [h(\alpha, \beta, \tau, v) - h(\alpha, \beta, \tau, \bar{v})] \\
 & \quad - \int_0^t [b(r)(2m)^2 + (2n)^2] dr \\
 & e^{\tau} \sin(2m\alpha) \sin(2n\beta) d\alpha d\beta d\tau \\
 & + \sum_{m,n=1}^{\infty} \frac{4}{\pi^2} \int_0^t \int_0^{\pi} \int_0^{\pi} h(\alpha, \beta, \tau, \bar{v}) \\
 & \quad \left( \begin{array}{c} - \int_0^t [b(r)(2m)^2 + (2n)^2] dr \quad - \int_0^t [\bar{b}(r)(2m)^2 + (2n)^2] dr \\ e^{\tau} \quad - e^{\tau} \end{array} \right) \\
 & \sin(2m\alpha) \sin(2n\beta) d\alpha d\beta d\tau
 \end{aligned}$$

$$\begin{aligned}
 \|v - \bar{v}\|_B & \leq \frac{\|\varphi_0 - \bar{\varphi}_0\|}{4} \\
 & + \sum_{m,n=1}^{\infty} \|\varphi_{cmn} - \overline{\varphi_{cmn}}\| + \|\varphi_{csmn} - \overline{\varphi_{csmn}}\| \\
 & + \|\varphi_{scmn} - \overline{\varphi_{scmn}}\| + \|\varphi_{smn} - \overline{\varphi_{smn}}\| \\
 & + \sqrt{T} \left( \frac{3\sqrt{\pi} + 16}{3\pi} \right) \|l(\alpha, \beta, \tau)\|_{L_2(\Gamma)} \|v(\tau) - \bar{v}(\tau)\|_B + \sqrt{T} \left( \frac{3\sqrt{\pi} + 16}{3\pi} \right) \|l(\alpha, \beta, \tau)\|_{L_2(\Gamma)} M \|b(\tau) - \bar{b}(\tau)\| \text{ where}
 \end{aligned}$$

$$\begin{aligned}
 \|\theta - \bar{\theta}\| & = \frac{\|\varphi_0 - \bar{\varphi}_0\|}{4} \\
 & + \sum_{m,n=1}^{\infty} \|\varphi_{cmn} - \overline{\varphi_{cmn}}\| + \|\varphi_{csmn} - \overline{\varphi_{csmn}}\| \\
 & + \|\varphi_{scmn} - \overline{\varphi_{scmn}}\| + \|\varphi_{smn} - \overline{\varphi_{smn}}\|.
 \end{aligned}$$

$$\|b(\tau) - \bar{b}(\tau)\|_{C[0,T]} \leq C \|v(\tau) - \bar{v}(\tau)\|_B$$

$$\text{where } C = \left( \frac{\pi M}{2\|u(\tau)\|_B \|\bar{u}(\tau)\|_B} + \frac{\pi \|l(\alpha, \beta, \tau)\|_{L_2(\Gamma)}}{2\|u(\tau)\|_B} \right)$$

$$\|v - \bar{v}\|_B^2 \leq 2D^2 \|\theta - \bar{\theta}\|^2 \times 0$$

$$D = \frac{1}{1 - \left( \sqrt{T} \left( \frac{3\sqrt{\pi} + 16}{3\pi} \right) \|l(x, y, t)\|_{L_2(\Gamma)} + MC \right)}$$

For  $\theta \rightarrow \bar{\theta}$  then  $v \rightarrow \bar{v}$ . Hence  $b \rightarrow \bar{b}$ .

#### 4. NUMERIC METHOD FOR THE PROBLEM

Let's linearize it for the nonlinear data in the problem:

$$u_t^{(n)} = b(\tau)u_{xx}^{(n)} + u_{yy}^{(n)} + h(\alpha, \beta, \tau, u^{(n-1)}), \quad (\alpha, \beta, \tau) \in \Gamma$$

$$u^{(n)}(\alpha, \beta, 0) = \varphi(\alpha, \beta), \alpha \in [0, \pi], \beta \in [0, \pi]$$

$$u^{(n)}(0, \beta, \tau) = u^{(n)}(\pi, \beta, \tau), \beta \in [0, \pi], \tau \in [0, T]$$

$$u^{(n)}(\alpha, 0, \tau) = u^{(n)}(\alpha, \pi, \tau), \alpha \in [0, \pi], \tau \in [0, T]$$

$$u_\alpha^{(n)}(0, \beta, \tau) = u_\alpha^{(n)}(\pi, \beta, \tau), \beta \in [0, \pi], \tau \in [0, T]$$

$$u_\beta^{(n)}(\alpha, 0, \tau) = u_\beta^{(n)}(\alpha, \pi, \tau), \alpha \in [0, \pi], \tau \in [0, T]$$

Let us  $u^{(n)}(\alpha, \beta, \tau) = v(\alpha, \beta, \tau)$  ve  $h(\alpha, \beta, \tau, u^{(n-1)}) = \bar{h}(\alpha, \beta, \tau)$ .

$$v_t = b(\tau)v_{xx} + v_{yy} + \bar{f}(\alpha, \beta, \tau), \quad (\alpha, \beta, \tau) \in \Gamma$$

$$v(\alpha, \beta, 0) = \varphi(\alpha, \beta), \alpha \in [0, \pi], \beta \in [0, \pi]$$

$$v(0, \beta, \tau) = v(\pi, \beta, \tau), \beta \in [0, \pi], \tau \in [0, T]$$

$$v(\alpha, 0, \tau) = v(\alpha, \pi, \tau), \alpha \in [0, \pi], \tau \in [0, T]$$

$$v_\alpha(0, \beta, \tau) = v_\alpha(\pi, \beta, \tau), \beta \in [0, \pi], \tau \in [0, T]$$

$$v_\beta(\alpha, 0, \tau) = v_\beta(\alpha, \pi, \tau), \alpha \in [0, \pi], \tau \in [0, T]$$

$[0, \pi]^2 \times [0, T]$  is divided to an  $M^2 \times N$  mesh with the step sizes  $h = \pi/M, \tau = T/N$ .

Let's take  $v_{i,j}^k, f_{i,j}^k, \varphi_i$  and  $b^k$  that instead of  $v(\alpha_i, \beta_j, \tau_k), h(\alpha_i, \beta_j, \tau_k), \varphi(\alpha_i, \beta_j)$  and  $b(\tau_k)$ , respectively.

Then we examine implicit finite-difference method for the last problem :

$$\frac{1}{\tau}(v_{i,j}^{k+1} - v_{i,j}^k) = \frac{1}{h^2} \left[ b^k (v_{i-1,j}^{k+1} - 2v_{i,j}^{k+1} + v_{i+1,j}^{k+1}) + (v_{i,j-1}^{k+1} - 2v_{i,j}^{k+1} + v_{i,j+1}^{k+1}) \right] + h_{i,j}^{k+1},$$

$$v_{i,j}^0 = \varphi_i,$$

$$v_{0,j}^k = v_{M+1,j}^k, v_{M+1,j}^k = \frac{v_{1,j}^k - v_{M,j}^k}{2}$$

$$v_{i,0}^k = v_{i,M+1}^k, v_{i,M+1}^k = \frac{v_{i,1}^k - v_{i,M}^k}{2}$$

If we take integral to  $x$  and  $y$  from  $0$  to  $\pi$ , we get,

$$b(\tau) = \frac{k'(\tau) - \int_0^\pi \int_0^\pi xy h(\alpha, \beta, \tau) d\alpha d\beta - \frac{\pi^3}{2} v_y(\pi, \tau)}{\frac{\pi^3}{2} v_x(\pi, \tau)}.$$

$$b^{k+1} = - \frac{\left( (k^{k+2} - k^k) / \tau \right)}{\left( \frac{\pi^3}{2} v_x(\pi, \tau) \right)^k} - \frac{\left( \int_0^\pi \int_0^\pi xy h(\alpha, \beta, \tau) d\alpha d\beta \right)^k}{\left( \frac{\pi^3}{2} v_x(\pi, \tau) \right)^k} - \left( \frac{\pi^3}{2} v_y(\pi, \tau) \right)^k$$

where  $k^k = k(t_k)$ ,  $k = 0, 1, \dots, N$ .

Here, Simpson's central difference scheme is applied.  $b^{k(s)}$ ,  $v_{i,j}^{k(s)}$  of  $b^k$ ,  $v_{i,j}^k$  at the  $s$ -th iteration step.

$$\frac{1}{\tau} (v_{i,j}^{k+1(s+1)} - v_{i,j}^{k+1(s)})$$

$$= \frac{1}{h^2} \left[ b^{k(s+1)} (v_{i-1,j}^{k+1(s+1)} - 2v_{i,j}^{k+1(s+1)} + v_{i+1,j}^{k+1(s+1)}) \right]$$

$$+ \left[ v_{i,j-1}^{k+1(s+1)} - 2v_{i,j}^{k+1(s+1)} + v_{i,j+1}^{k+1(s+1)} \right]$$

$$+ h_{i,j}^{k+1},$$

$$v_{i,j}^0 = \varphi_i,$$

$$v_{0,j}^{k+1(s)} = v_{M+1,j}^{k+1(s)}, v_{M+1,j}^{k+1(s)} = \frac{v_{1,j}^{k+1(s)} - v_{M,j}^{k+1(s)}}{2}$$

$$v_{i,0}^{k+1(s)} = v_{i,M+1}^{k+1(s)}, v_{i,M+1}^{k+1(s)} = \frac{v_{i,1}^{k+1(s)} - v_{i,M}^{k+1(s)}}{2}$$

$v_{i,j}^{k+1(s+1)}$  is found.

## 5. CONCLUSION

The inverse problem of defining thermal dissipation and the heat in the semi-linear two-dimensional parabolic equation with periodic boundary and integral conditions is investigated. The problem has been studied both theoretically and numerically. In this article, periodic boundary conditions are studied. Nonlocal Periodic boundary conditions for heat inverse coefficient problems are more difficult than local boundary conditions. In this study, the results were obtained by using the Fourier method and the finite difference method.

## 6. ACKNOWLEDGMENTS

We would like to thank the reviewers.

## 7. REFERENCES

1. Sharma, P.R., Methi, G. (2012). Solution of two-dimensional parabolic equation subject to non-local conditions using homotopy Perturbation method, Jour. of App.Com., 1, 12-16.
2. Cannon, J. Lin, Y. (1899). Determination of parameter p(t) in Hölder classes for some semi linear parabolic equations, Inverse Problems, 4, 595-606.
3. Dehghan, M. (2005). Efficient techniques for the parabolic equation subject to nonlocal specifications, Applied Numerical Mathematics, 52(1), 39-62,2005.
4. Dehghan, M. (2001). Implicit Solution of a Two-Dimensional Parabolic Inverse Problem with Temperature Overspecification, Journal of Computational Analysis and Applications, 3(4).
5. Bağlan, I., Kanca, F. (2020). Solution of the boundary-value problem of heat conduction with periodic boundary conditions, Ukrainian Mathematical Journal, 72(2), 232-245.

6. Bađlan, I., Kanca, F. (2020). Two-dimensional inverse quasilinear parabolic problems with periodic boundary conditions of the boundary-value problem of heat conduction with periodic boundary conditions, *Applicable Analysis*, 98(8), 1549-1565.
7. Ionkin, N.I. (1977). Solution of a boundary value problem in heat conduction with a nonclassical boundary condition, *Differential Equations*, 13, 204-211.
8. Hill G.W. (1886), On the part of the motion of the lunar perigee which is a function of the mean motions of the sun and moon, *Acta Mathematica*, 8,1-36.

IDUNAS	NATURAL & APPLIED SCIENCES JOURNAL	2023 Vol. 6 No. 1 (21-28)
--------	---------------------------------------	------------------------------------

## Investigation of the Strength Behavior of a Fuselage Structure Placed In a Linearly Expanding Wing With Circular Ends In Cross-Section

Research Article

M.Murat YAVUZ<sup>1\*</sup> , Beril ÇİNERİ<sup>1\*</sup> ,

<sup>1</sup>Assist.Prof.Dr., İzmir Democracy University, Faculty of Engineering, Mechanical Engineering Department.

Author E-mails

[murat.yavuz@idu.edu.tr](mailto:murat.yavuz@idu.edu.tr)

[berilciner@gmail.com](mailto:berilciner@gmail.com)

\*Correspondence to: M. Murat Yavuz, Department of Mechanical Engineering, Izmir Democracy University, Izmir, Turkey.  
DOI: 10.38061/idunas.1039891

Received: 22.12.2022; Accepted: 27.06.2023

### Abstract

In this study, a structurally different drop wing geometry was modelled and its mechanical behavior was investigated with computer aided analysis software within the finite element method. The tip of the drop wing geometry consists of one large and the other small circles. There were linear line profiles between them. In order to prevent collapse in the wing geometry modelled with the plate structure, a profile in the rigid body structure was created and its effect was investigated. The effect of the wing length and the plate thickness covering the wing was examined and shown in the results. It was defined as the profile material for the wing made of steel and for the standard features. In the static examinations carried out under the pressure loading applied on the wing, it was determined that the vertical deformation caused by the wing length was not linear, and the stresses that occur with the increasing wing plate thickness form a decreasing function. The stresses that occur in the inside of the wing support were intense in the support area, but also in the bending areas.

**Keywords:** Wing, Plate, Surface pressure, Stress.

## 1. INTRODUCTION

The wing is the fundamental component that humans have studied and refined since the dawn of time in order to give them the ability to fly. Wings are generally utilized in glider-style constructions, which resemble rudimentary airplane structures that allow gliding and are inspired by birds. As a result of the development phase, it was merged with the engine part and acquired its current aircraft form once it was realized that flying with human power was challenging. The aerodynamic performance that improves the flight condition is the most crucial wing design parameter. Under operational circumstances, it must also offer a few mechanical qualities. Numerous studies have generally been built around figuring out the ideal weight and strength ratios.

The effect of wing thickness and geometry to reduce weight on the wing [1] was investigated by considering aerodynamic/structural features in combination. In the hybrid structure [2], wing design methods capable of multiple optimization were investigated and a multi-purpose genetic algorithm was developed. Different structures suitable for the 2D and 3D wing profile [3] structure have been designed with the appropriate optimization method and a great deal of savings has been achieved. An airplane [4] in the wing body structure for transonic airplanes is designed with computer aided flow analysis and constrained inverse design method. Wing body design [5] for subsonic transport has also been examined and a reduction in weight has been achieved with an increase in performance. The aerodynamic shape structure of a wing was investigated, and its control was studied for two cases with and without load reduction [6].

In the research that demonstrated improvement, ideal outcomes were established. Using a parametric examination method, Jiapeng et al. [7] created a quick modeling process for the structural design of a wing. The varied fiber orientations and layer thicknesses of an aircraft composite sheet in bending state were studied by Rajappan and Pugazhenti in 2013 [8]. A wing with a variable camber structure has been created [9], and attributes that can reduce noise and save fuel have been attained. A method that can adhere to the design requirements on the model has been established for the optimization method [10], and an improvement in performance has been made in the design.

A new wing design was created by evaluating the literature information and the interaction between the plate and the wing profile was investigated.

## 2. MATERIAL AND METHOD

In order to carry out the study, a general wing profile was created with a computer aided drawing program. This aerofoil is modelled symmetrically in a linear section structure, not used in standard airplanes and not in a way to form a higher protrusion on one surface. A solid body profile is placed inside the wing model. With this model, which is not in the standards, it is investigated how the plate-solid body interaction affects the wing. In Figure 1, basic geometric information for the wing is shown. Its wingspan is 100 mm and its length is basically 200 mm. The front and rear ends are modelled as circular with radiuses of 20 mm and 10 mm, respectively. The wing is modelled as a plate and its thickness is 1 mm. The thickness of the structure used for support in the inner section is 1 mm. For the wing in the figure, a pressure of 1000 Pa was applied only from its upper surface. One end of the wing and profile structure is fixed to form a support. The interaction between the plate forming the wing and the inner section structure is in the frictional surface structure. There is a relative interaction between the two structures, depending on Columb's law of friction. The friction coefficient was used as 0.3.



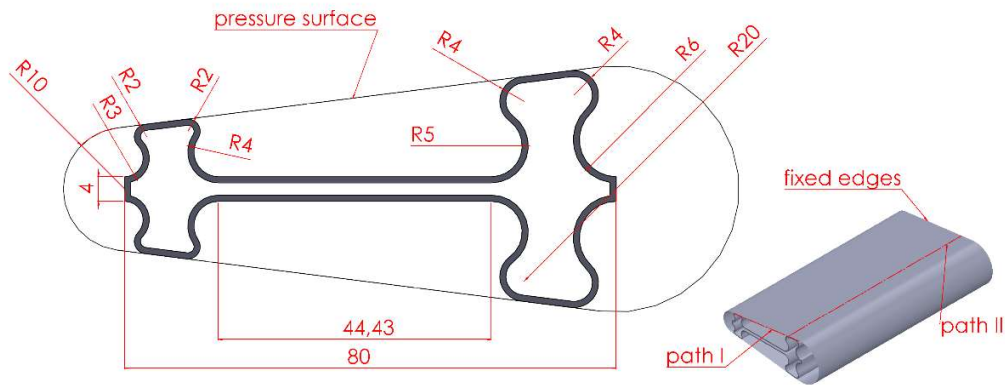


Figure 1. Wing geometry and dimensions

For the results, a path was created on the free section edge of the wing and the deformation and stresses related to the wing were taken over this path and graphed. For the profile structure in the inner section, a line called “path II” was created and the profile deformation was shown. Stress results are given in Von-Mises stress type.

$$\sigma_{VM} = \sqrt{\frac{(\sigma_1 - \sigma_2)^2 + (\sigma_2 - \sigma_3)^2 + (\sigma_3 - \sigma_1)^2}{2}} \quad (1)$$

### 3. RESULTS AND DISCUSSIONS

The analysis's findings have no dimensions in order to highlight the impact of unit length. Path I in Fig. 2 illustrates the vertical deformation. Cross-section lines are used to indicate the areas where the plate makes contact with the support platform. Below the vertical axis, a negative deformation distribution is shown as a result of the downward pressure imparted across the wing. It has been found that the distortion increases as wing length increases. Deformation in the contact region behind the section began to slow down, but it suddenly accelerated in the front of the section.

The incoming deformation distribution is similar in all results. However, the place where the highest deformation occurs moves towards the back corner of the section as a result of the increasing l/b ratio. Increasing the l/b ratio from 2 to 3 nearly doubled the maximum deformation value. However, increasing the l/b ratio from 2 to 4 caused a deformation increase more than 3 times compared to the first case. Therefore, although the distribution was similar, the rate of increase did not occur linearly.

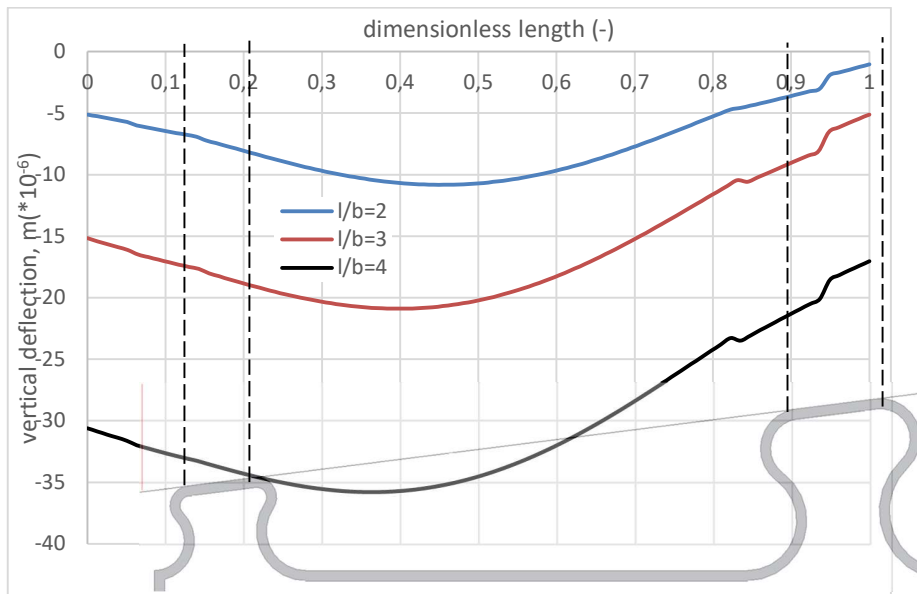


Figure 2. “Deformations in the vertical direction according to the wing length/width ratio on the path I line

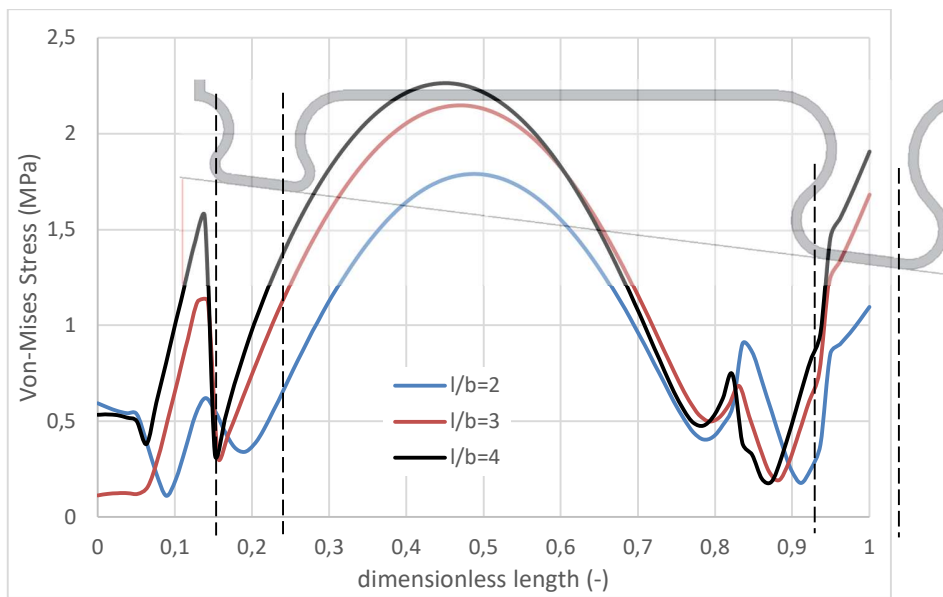
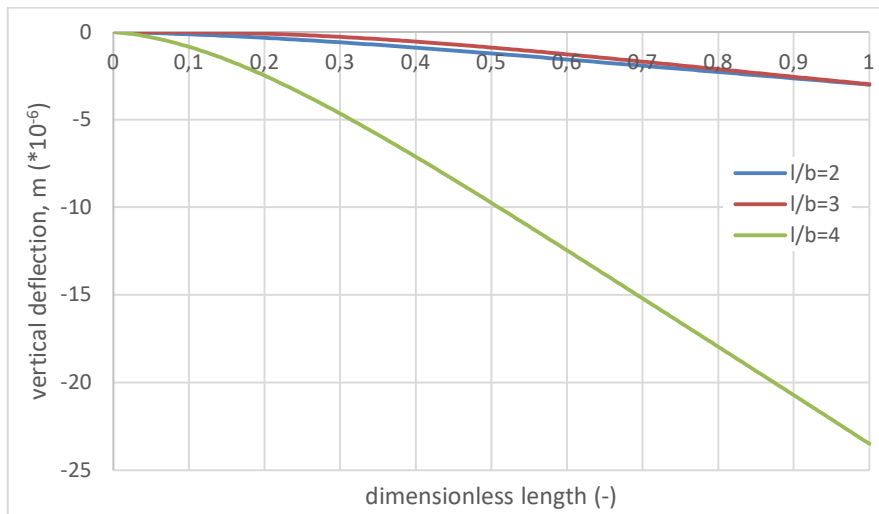


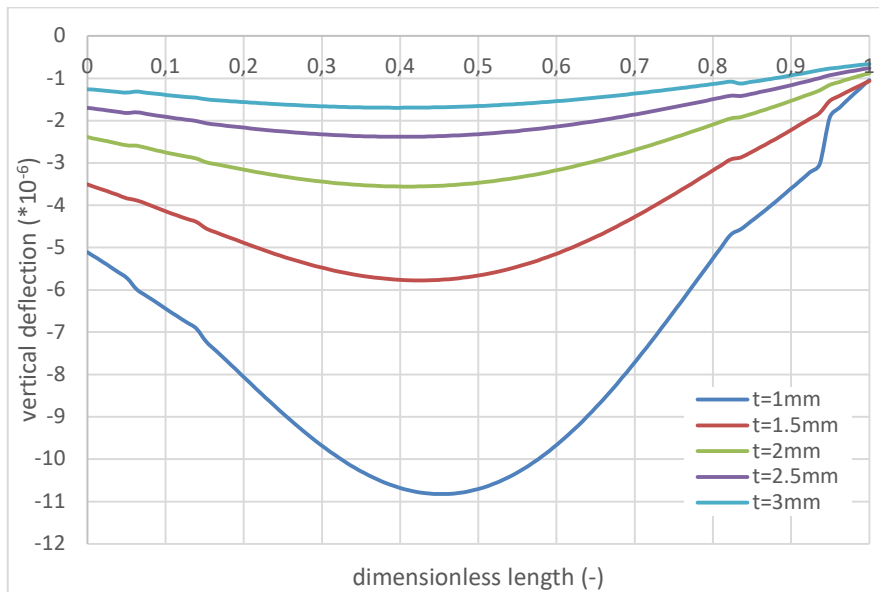
Figure 3. Stresses on the path I line according to the wing length/width ratio

Figure 3 shows the stress distribution on path I. The stress distribution was formed as 3 high value regions in all results, with the largest value in the middle part. These regions where the stresses intensified and increased/decreased abruptly occurred in the areas where the in-wing platform was in contact. The difference ratio between the highest values was less than the deformation difference ratio in the vertical direction. The region with the highest value moved towards the back of the wing as a result of the increasing  $l/b$  ratio.



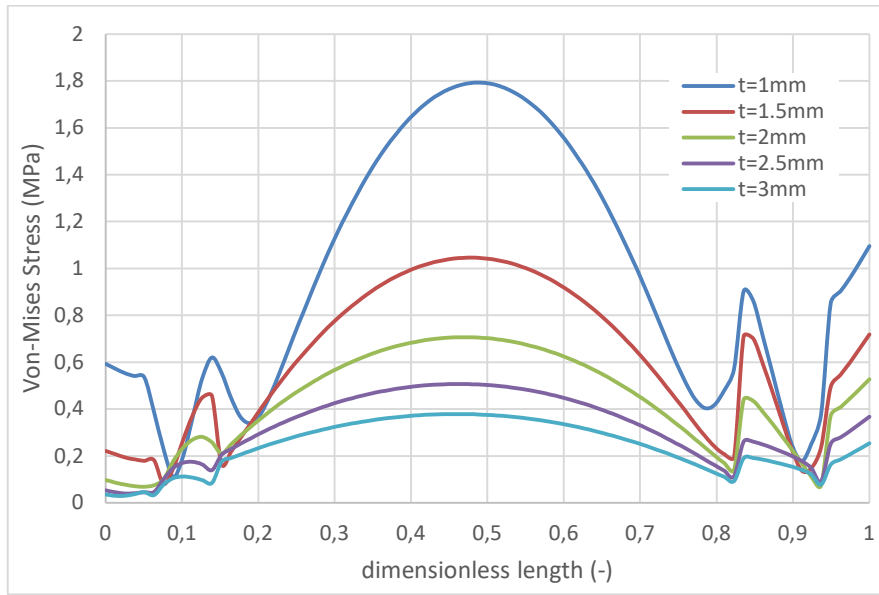
**Figure 4.** Deformation in the vertical direction according to the wing length/width ratio on the path II line

In Fig. 4, the deformation results in the vertical direction over the platform from the path II line are taken. In the results showing the dimensionless length fixed support behavior, the difference between the results for the l/b ratio 2 and 3 was small. However, the deformation is very high for the l/b ratio of 4. The reason for this is the fact that more shear-related deformation occurs at the free end of the blade as a result of the increased length.



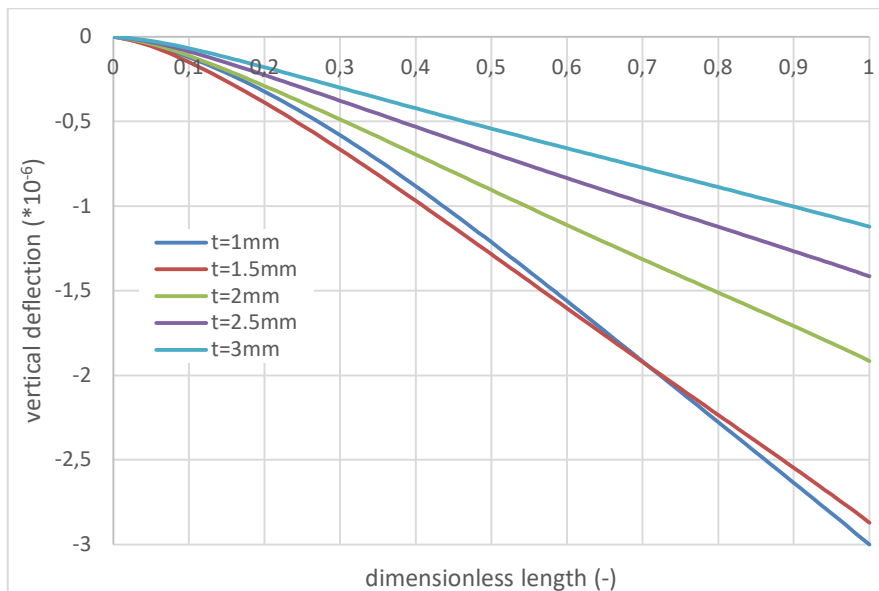
**Figure 5.** Deformation in the vertical direction according to the wing length/width ratio on the path I line

For l/b=2 ratio, deformation values are shown in Fig. 5 for plate results with different thickness than path I position. Each part of the homogeneously formed plate is of equal thickness. Although the deformation distribution did not change as a result of increasing thickness, the values were formed as a decreasing equation.



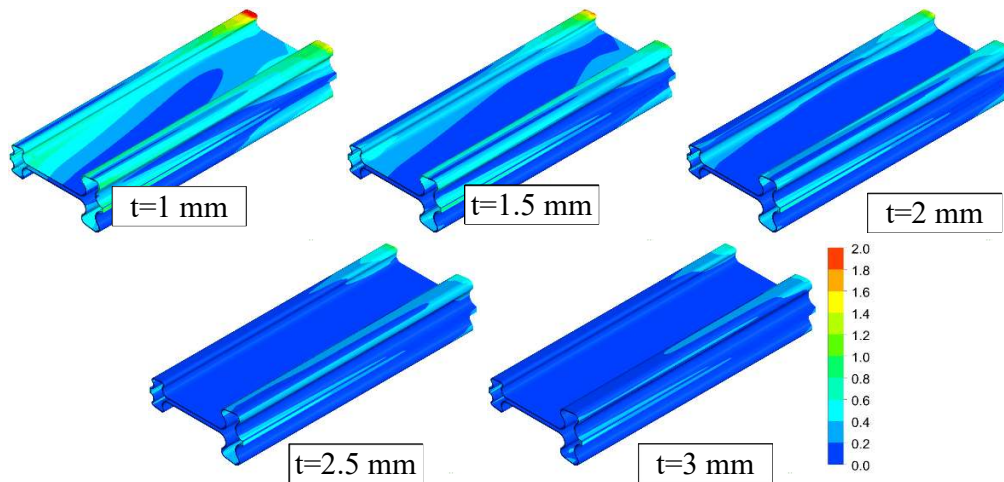
**Figure 6.** Stresses on the path I line according to the wing length/width ratio

Fig. 6 shows the stresses occurring at the path I location. The tensile value decreased from 1.8 MPa to 0.4 MPa as a result of increasing thickness. The general distribution is similar. The values on the right side of the stress intensities are greater than the values on the left side, except for the center region where the highest stress occurs. The reason for this can be shown as the larger circular tip and in-wing profile area at the front end of the wing.



**Figure 7.** Deformation in the vertical direction according to the wing length/width ratio on the path II line

In Fig. 7, the deformation structure formed on path II is shown for different plate thicknesses. The geometric toughness resulting from the increased thickness reduced the deformation. A non-linear ratio occurred between the reduction rate and the thickness.



**Figure 8.** Stresses in the wing support profile

Von-Mises stress distributions caused by different thicknesses are shown in figure 8 for the aerofoil. With increasing thickness, the stress values decreased, and the stress regions formed at high values became smaller. The places where the highest stresses occur are in the support region. In addition, the places where the geometry direction changes in the bending places of the profile seem to be regions where high stresses occur.

## 5. CONCLUSIONS

In this project, a 3D model of a wing section was created. An in-wing platform was made for support because the shape of the model is a plate in a thin shell structure. These constructions represent the wing part in the overall structure, despite the lack of a specific standard. To sum up some data regarding the wing design that is being studied in terms of static bending state;

- It was observed that the wing deformation increased as a result of increasing wing length and it was determined that this increase was not linear.
- High stress values were observed at the edges of the contact area of the support platform and in the middle of the wing.
- While increasing wing length causes a dominant increase in the deformation value, this increase in the stress value is at a lesser level.
- While similar results were obtained for the wing length-width ratios 2 and 3 in the deformation of the wing support profile, a 4-fold ratio causes high deformation.
- Increasing thickness value changed the deformation and stress values as a decreasing function.
- The stresses have generally occurred in the support area and bending places of the profile.

## 6. REFERENCES

- [1] Grossman, B., Gurdal, Z., Strauch, G. J., Eppard, W. M., Haftka, R.T. (1988). Integrated aerodynamic/structural design of a sailplane wing. *Journal of Aircraft*, 25(9), 855-860.
- [2] Vicini, A., Quagliarella, D. (1999). Airfoil and wing design through hybrid optimization strategies. *AIAA Journal*, 37(5), 634-641.
- [3] Alexandrov, N., Lewis, R., Gumbert, C., Green, L., Newman, P. (2000). Optimization with variable-fidelity models applied to wing design, *AIAA 2000-841, 38th Aerospace Sciences Meeting and Exhibit*. January 2000.
- [4] Potsdam, M., Page, M., Liebeck, R., Potsdam, M., Page, M., Liebeck, R. (1997). Blended wing body analysis and design. *AIAA 1997-2317, 15th Applied Aerodynamics Conference*, June 1997.
- [5] Liebeck, R. H. (2004). Design of the blended wing body subsonic transport. *Journal of Aircraft*, 41(1), 10-25.
- [6] Haghghat, S., Martins, J. R. R. A., Liu, H. H. T. (2012). Aeroservoelastic design optimization of a flexible wing. *Journal of Aircraft*, 49(2), 432-443.
- [7] Jiapeng, T., Ping, X., Baoyuan, Z., Bifu, H. (2013). A finite element parametric modeling technique of aircraft wing structures. *Chinese Journal of Aeronautics*, 26(5), 1202–1210.
- [8] Rajappan, R., Pugazhenth, V. (2013). Finite element analysis of aircraft wing using composite structure. *The International Journal of Engineering and Science (IJES)*, 2(2), 74-80.
- [9] Joo, J. J., Marks, C. R., Zientarski, L., Culler, A. J. (2015). Variable camber compliant wing – design. *23rd AIAA/AHS Adaptive Structures Conference, AIAA 2015-1050*, January 2015.
- [10] Bartoli, N., Lefebvre, T., Dubreuil, S., Olivanti, R., Priem, R., Bons, N., Martins, J. R. R. A., Morlier, J. (2019). Adaptive modeling strategy for constrained global optimization with application to aerodynamic wing design. *Aerospace Science and Technology*, 90, 85-102.

<b>IDUNAS</b>	<b>NATURAL &amp; APPLIED SCIENCES JOURNAL</b>	2023 Vol. 6 No. 1 (29-40)
---------------	---	------------------------------------

# Cold Pressed Pure Aluminum Powders Sintering With Ultra High Frequency Induction

Research Article

Hıdır Sercan Çubuk<sup>1</sup> , Tural Ege Ertaş<sup>2</sup> , Uğur Çavdar\*<sup>3</sup> 

<sup>1</sup>İzmir Demokrasi University, Graduate School of Natural and Applied Sciences, Mechanical Engineering Program, 35580 İzmir, Turkey

<sup>2</sup>İzmir Demokrasi University, Faculty of Engineering, Mechanical Engineering Department, 35580 İzmir, Turkey

<sup>3</sup>\*İzmir Demokrasi University, Faculty of Engineering, Mechanical Engineering Department, 35580 İzmir, Turkey

Author E-mails

ugur.cavdar@idu.edu.tr

\*Correspondence to: İzmir Demokrasi University, Faculty of Engineering, Mechanical Engineering Department, 35580 İzmir, Turkey

DOI: 10.38061/idunas.1310506

Received: 06.06.2023; Accepted: 27.06.2023

## Abstract

Metals both have good mechanical and electrical qualities, besides, they are also created as light as possible by using recent manufacturing techniques. In that scope, this study aims to use an ultra-high frequency sintering technique to sinter aluminum powders of 15 µm in size. A mold and 30 bar pressure were used to compress the powders before sintering. For the sintering temperature optimization, 3 experiments were conducted in the induction system at 600°C, 650°C, and 700°C temperatures. Sintering conditions were determined at different time intervals of 3 minutes, 5 minutes, and 10 minutes to find an optimum value for sintering time. Finally, furnace sintering was used for 1 hour at these temperatures. With 2 different sintering, 3 different temperatures, and 3 different time parameters, size, density, porosity, and hardness values were obtained. Obtained results were compared among themselves.

**Keywords:** Induction, Aluminum, Sintering, Hardness

## 1. INTRODUCTION

Aluminum (Al) and aluminum alloy materials are among the most important metals in today's industry. It is necessary to conduct a further investigation of the aluminum materials. Besides the low density, its electrical conductivity [1] requires comprehensive research to improve its mechanical properties through alloying or various manufacturing methods. Since it is a recyclable metal, there is a rapid increase in the use of aluminum in various industries [2,3]

Powder metallurgy (PM) covers the production and assembly of powder metal parts that can be refined or homogeneous [4,5]. However, the difficulties that may arise during the sintering of light metals such as

aluminum pave the way for creating a new field of study in traditional powder metallurgy technologies. Besides investigating alloying elements in pressing and sintering processes, applying and discovering the advantages of fast production techniques such as induction is also important. Regarding the further studies, the obtained strength and density values can be improved [6-8].

Induction is a much faster heat treatment method than the furnace [8-10]. Performing the sintering process by induction in a material with electrical conductivity is based on the principle of a vortex flow [10]. Vortex flow allows the determination of the depth, called the 'depth of penetration,' on the material's exterior surface. In this process, one of the most important parameters is the frequency of the induction device [10-12]. Even though the devices are easy to maintain, the induction sintering process is used for smaller samples than it is used for conventional furnaces. The induction sintering process provides rapid heating, reducing sintering times and providing energy efficiency [10]. Induction hardening or heat treatment is used to improve the mechanical properties of metals such as aluminum. In the hardening process, various parameters are taken into consideration [11-16]. Induction hardening is an important manufacturing process to control the mechanical properties of metal parts. It controls an increase in surface hardness while maintaining the core original structure and toughness properties. Appropriate phase transformation in the exterior surface of the material is possible by inducing [17-22].

This study investigated the effects of induction and furnace sintering applied to pure aluminum powders at different times and temperatures after cold pressing. It is found that the values of the density, size, hardness and porosity of the samples and the results were compared among themselves.

## 2. MATERIALS & METHODS

### 2.1. Material

In this experiment, the environment is at room temperature. After the literature review, material and molds were provided, and conditions were determined for the experiment. The aluminum powders used are spherical micron powders with a purity of 98.85%. It is produced by the gas atomization method. The average particle size of the powders is approximately 15 μm, the molecular weight is 26.98 g/mol, and the density is 2.7 g/m<sup>2</sup>. The chemical content of aluminum powder is given in Table 1.

**Table 1.** Chemical Composition of Pure Aluminum Powder

<i>Component (Max)</i>	<i>Al</i>	<i>Fe</i>	<i>Si</i>	<i>Cu</i>	<i>Zn</i>	<i>Ti</i>
<i>Weight %</i>	98.85	0.50	0.35	0.15	0.08	0.07

A single-axis single-effect mold was used for the compaction of powder mixtures. 30 bar pressure was used to press to compact the powdered material. The mold is made of an alloy-hardened steel cylinder. The outer diameter of the mold is 56mm, the height is 60mm, and the outer diameter of the penetrating punch is 16mm. Figure 1 shows a photograph of a single-axis single-effect mold. On the other hand, the induction device is an Ultra High-Frequency Induction Device that works with 20% power with 2.8 kW, 900 kHz. The induction coil is a single wounded. Its outer diameter is 26mm, and its wall thickness is 0.5mm.



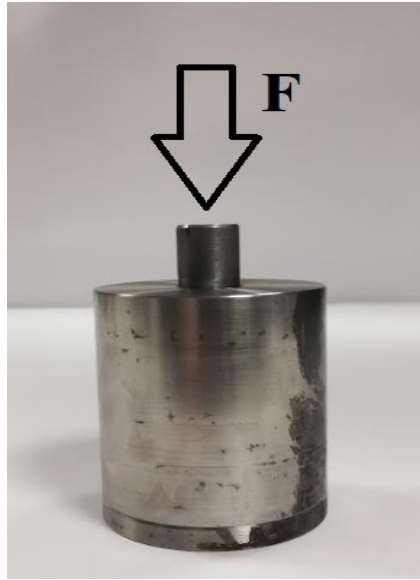


**Figure 1.** A Single-Axis Single-Effect Mold and Applied Force

## 2.2. Method

Al powders were pressed as 2.50 grams' packages. A press device was used to supply the powder as a compacted sample. Pressing was done in a single-axis single-acting press under 30 bar pressure. The raw sample dimensions were formed in a coin-like shape approximately 16mm in diameter and 2mm in height (E.R. [Error Range]  $\pm 0.3\%$ ). After providing the raw material, 9 samples were subjected to the induction sintering process. To optimize the sintering temperature, the induction system was run at 3 different temperatures at 600°C, 650°C, and 700°C. For the sintering time optimization, appropriate values for sintering conditions were determined at time intervals of 3 minutes, 5 minutes, and 10 minutes. The sintering process was run in the furnace for 60 minutes. After the sintering process, all samples were cooled naturally. Figure 2 shows the samples that are prepared for sintering. Besides, the parameters applied to pure aluminum are shown in Table 2 and the process steps in Table 3.

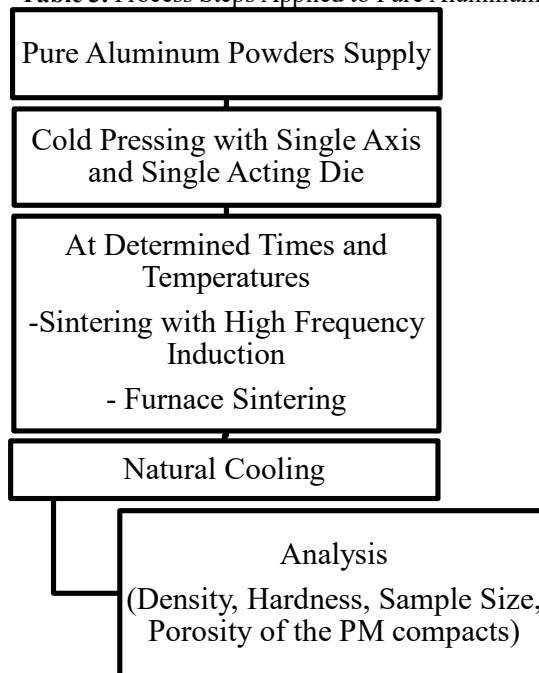


**Figure 2.** Samples Prepared for Sintering

**Table 2.** Parameters of Pure Aluminum Sintering Process

No.	Al	Sintering Process	Heat-treated Time (min)	Pressure Applied in Cold Press (Bar)	Heat (°C)
1	Pure Al	Induction	3	30	600
2	Pure Al	Induction	5	30	600
3	Pure Al	Induction	10	30	600
4	Pure Al	Induction	3	30	650
5	Pure Al	Induction	5	30	650
6	Pure Al	Induction	10	30	650
7	Pure Al	Induction	3	30	700
8	Pure Al	Induction	5	30	700
9	Pure Al	Induction	10	30	700
10	Pure Al	Furnace	60	30	600
11	Pure Al	Furnace	60	30	650
12	Pure Al	Furnace	60	30	700

**Table 3.** Process Steps Applied to Pure Aluminum



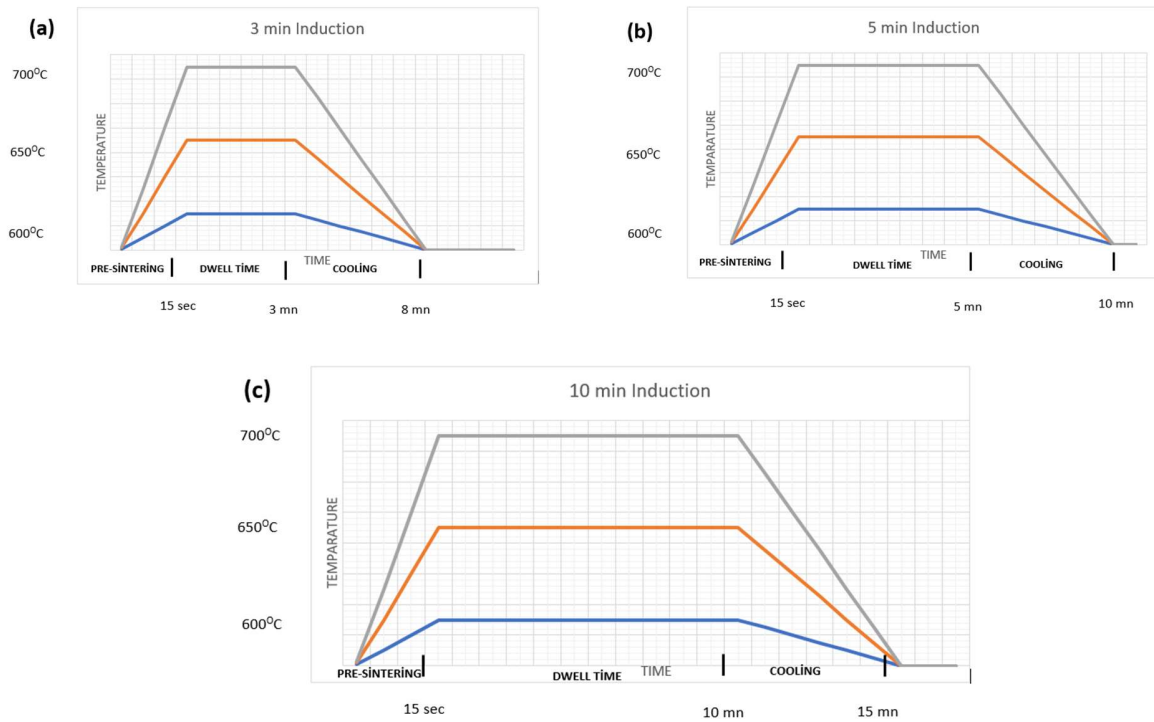


Figure 4. Temperature time graph of the induction process in 3min (a) , 5 min (b) , and 10 min (c)

### 3. FINDINGS

#### 3.1. Density Values

Raw density and sintered density values of pure aluminum, sintered with an induction device operating at 20 percent power at 600°C, 650°C, and 700°C at different induction times, are given in Table 4. The raw density refers to the density of the raw material after it is printed in the mold, and the sintered density refers to the density measured after induction.

Table 4. Density Change According to Temperature and Time Parameters as a Result of Sintering of Pure Aluminum in Induction Device

SAMPLE NO	HEAT (°C)	TIME (min)	RAW DENSITY (g/cm <sup>3</sup> )	SINTERED DENSITY (g/cm <sup>3</sup> )	CHANGE (%)
1	600°C	3 min	2.550	2.603	2.054
2	600°C	5 min	2.563	2.621	2.254
3	600°C	10 min	2.543	2.596	2.103
4	650°C	3 min	2.536	2.578	1.644
5	650°C	5 min	2.556	2.593	1.463
6	650°C	10 min	2.521	2.552	1.257
7	700°C	3 min	2.546	2.574	1.103
8	700°C	5 min	2.536	2.562	1.028
9	700°C	10 min	2.583	2.610	1.045

The findings in Table 4 show that the induction sintered sample has a higher density than the raw sample. For example, while the raw density was  $2.55 \text{ g/cm}^3$ , the final density of the sintered sample in the induction system at  $600^\circ\text{C}$  for 3 minutes was  $2.60 \text{ g/cm}^3$ . Besides, the density of the raw material before the sintering process was  $2.53 \text{ g/cm}^3$ . After being sintered in the induction system at  $700^\circ\text{C}$  for 5 minutes, the final density was measured as  $2,56 \text{ g/cm}^3$ . This increase was observed in all samples. The error range of the density values in the samples are approximately  $\pm 1.5\%$ . Table 5 shows the raw densities and post-sintering density values kept separately at  $600^\circ\text{C}$ ,  $650^\circ\text{C}$ , and  $700^\circ\text{C}$  for 1 hour.

**Table 5.** Density Change Caused by Sintering of Pure Aluminum at Different Temperatures in the Furnace

SAMPLE NO	HEAT ( $^\circ\text{C}$ )	TIME (min)	RAW DENSITY ( $\text{g/cm}^3$ )	SINTERED DENSITY ( $\text{g/cm}^3$ )	CHANGE (%)
10	$600^\circ\text{C}$	60 min	2.581	2.639	2.234
11	$650^\circ\text{C}$	60 min	2.570	2.498	-2.812
12	$700^\circ\text{C}$	60 min	2.556	2.466	-3.501

In Table 5, it is seen that the density of the sample sintered for 1 hour in the furnace at  $600^\circ\text{C}$  increased compared to its raw density, while the densities of the samples sintered for 1 hour in the furnaces at  $650^\circ\text{C}$  and  $700^\circ\text{C}$  decreased after sintering. Melting of the material and loss of mass causes a decrease in density, as shown in Figure 4. While the density increases by 2.23% at  $600^\circ\text{C}$ , it decreases by 2.81% at  $650^\circ\text{C}$  and 3.50% at  $700^\circ\text{C}$ .



**Figure 3.** Furnace Sintered at  $650^\circ\text{C}$  (Left), Sintered at  $700^\circ\text{C}$  (Right) Relatively Molten Pure Aluminum

### 3.2. Size Change

In Table 6, the raw and post-sintering sizes of the aluminum sintered at different time intervals as 3 minutes, 5 minutes, and 10 minutes operating at 600°C, 650°C, and 700°C, are given.

**Table 6.** Size Change as a Result of Induction Sintering of Pure Aluminum

SAMPLE NO	HEAT (°C)	TIME (min)	RAW SIZE (mm)	SINTERED SIZE (mm)	CHANGE (%)
1	600°C	3 min	16.15	16.10	-0.309
2	600°C	5 min	16.15	16.10	-0.309
3	600°C	10 min	16.25	16.20	-0.307
4	650°C	3 min	16.25	16.20	-0.307
5	650°C	5 min	16.25	16.20	-0.307
6	650°C	10 min	16.25	16.20	-0.307
7	700°C	3 min	16.20	16.15	-0.308
8	700°C	5 min	16.20	16.15	-0.308
9	700°C	10 min	16.20	16.15	-0.308

Table 6 shows that the diameter dimensions of the samples have decreased. For instance, while the raw size of the sample sintered at 650°C in 10 minutes is 16.25 mm, the size decreases to 16.20 mm after sintering. The error range was measured as max ±3.25%. Table 7 gives the size change values of the material sintered for 1 hour in the furnace at 600°C, 650°C, and 700°C.

**Table 7.** Size Change Due to Sintering of Pure Aluminum in the Furnace

SAMPLE NO	HEAT (°C)	TIME (min)	RAW SIZE (mm)	SINTERED SIZE (mm)	CHANGE (%)
10	600°C	60 min	16.20	16.20	0.000
11	650°C	60 min	16.15	15.95	-1.238
12	700°C	60 min	16.25	15.95	-1.846

Table 7 shows that while no change is observed at 600°C, a decrease is observed at values close to and above the melting temperature. The reason for the difference in decrease rates depends on the approaching and exceeding the melting temperature in the sintering material, as shown in Figure 4. According to that percentage of change increases which is also seen in the change in porosity values.

### 3.3. Hardness Results

Hardness values of pure aluminum sintered by ultra-high frequency induction at 600°C, 650°C, and 700°C for 3 minutes, 5 minutes, and 10 minutes are given in Table 8. Hardness was measured by taking the average of the 5 determined points. The determined points were set as the outermost of the circular part (200 µm inside the border), the center (8000 µm inside the border), and the middle of these two points (4000 µm inside the border).

**Table 8.** Hardness Change of Induction Sintered Pure Aluminum in Time and Temperature Parameters

SAMPLE NO	HEAT (°C)	TIME (min)	HARDNESS OF THE SINTERED EXTERIOR SURFACE (HV)	HARDNESS OF THE SINTERED MIDDLE SURFACE (HV)	HARDNESS OF THE SINTERED INSIDE (HV)
			<i>Distance: 200µm</i>	<i>Distance: 4000µm</i>	<i>Distance:8000 µm</i>
1	600°C	3 min	42.5	41.4	40.9
2	600°C	5 min	43.2	42.1	41.5
3	600°C	10 min	41.9	41.2	40.5
4	650°C	3 min	38.1	37.5	36.9
5	650°C	5 min	39.7	39.2	38.7
6	650°C	10 min	38.3	37.8	37.5
7	700°C	3 min	38.0	37.4	36.8
8	700°C	5 min	39.0	38.5	37.8
9	700°C	10 min	38.3	37.6	37.1

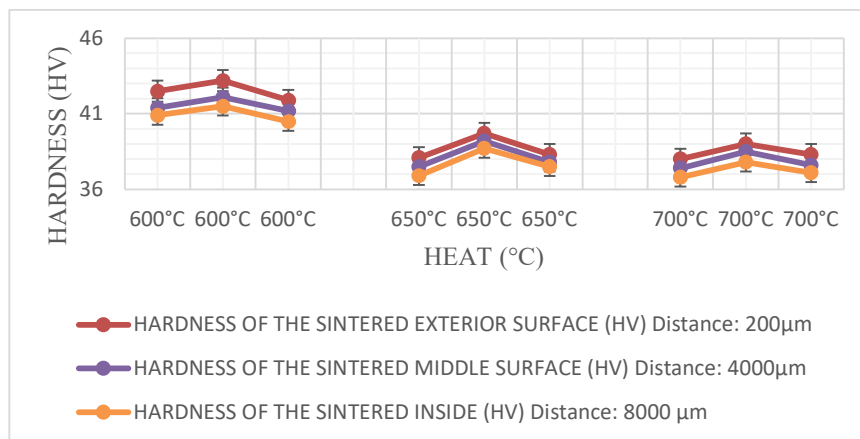


Figure 5. Density Change Caused by Sintering of Pure Aluminum at Different Temperatures in the Furnace

The values that are shown in Table 8 formed the curve as a parabolic curve. The hardness decreases if the time is kept constant and the temperature increases. Besides that, a comparison between 5 and 10 minutes shows that the hardness decreases as the temperature increases. The error range was found as ±2.25%. In Table 9, hardness values of pure aluminum sintered for 1 hour (60 minutes) in the furnace at 600°C, 650°C, and 700°C are given.

Table 9. Hardness Change of Pure Aluminum Sintered in the Furnace for 1 Hour

SAMPLE NO	HEAT (°C)	TIME (min)	HARDNESS OF THE SINTERED EXTERIOR SURFACE (HV)	HARDNESS OF THE SINTERED MIDDLE SURFACE (HV)	HARDNESS OF THE SINTERED INSIDE (HV)
			<i>Distance: 200µm</i>	<i>Distance: 4000µm</i>	<i>Distance: 8000 µm</i>
10	600°C	60 min	37.0	35.2	34.0
11	650°C	60 min	35.7	34.1	33.5
12	700°C	60 min	35.2	33.5	33.0

Table 9 shows that if the time is kept constant, the hardness decreases as the temperature increase. While the change in hardness between the sample sintered at 600°C and at 650°C is approximately ±1.3 (distance: 200µm), the change in hardness between the sample sintered at 650°C and at 700°C is ±0.5 (distance: 200µm).

### 3.4. Porosity Values

Raw porosity and post-sintering porosity values of pure aluminum sintered at 600°C, 650°C, and 700°C are given in Table 10.

**Table 10.** Raw and Sintered Porosity Values by Sintering Method and Time Parameters

SAMPLE NO	SINTERING METHOD	HEAT (°C)	TIME (min)	RAW POROSITY (g/cm <sup>3</sup> )	SINTERED POROSITY (g/cm <sup>3</sup> )	CHANGE (%)
1	Induction	600°C	3 min	0.056	0.036	-35.714
2	Induction	600°C	5 min	0.051	0.030	-41.176
3	Induction	600°C	10 min	0.059	0.039	-33.898
4	Induction	650°C	3 min	0.061	0.046	-24.590
5	Induction	650°C	5 min	0.054	0.040	-25.925
6	Induction	650°C	10 min	0.067	0.055	-17.910
7	Induction	700°C	3 min	0.058	0.047	-18.965
8	Induction	700°C	5 min	0.061	0.051	-16.393
9	Induction	700°C	10 min	0.044	0.034	-22.727
10	Furnace	600°C	60 min	0.044	0.023	-47.727
11	Furnace	650°C	60 min	0.048	0.075	56.249
12	Furnace	700°C	60 min	0.054	0.087	61.111

In Table 10, it is seen that the porosity decreases in the samples sintered by induction. Besides, the porosity of samples sintered with the furnace at 600°C decreases, and the final porosity value increases at 650°C and 700°C. While the change between the raw and post-sintering porosity values was approximately ±0.03, the porosity value change was approximately ±0.01 in the sample sintered at 700°C for 5 minutes. The average error range is found as ±1.3%.

In the literature, it is clear that there is a need for further investigation on the sintering of Pure Al powders by ultra-high frequency induction. In this study, it is shown that properties such as hardness can be increased by using faster manufacturing methods of aluminum. In future studies, experiments can be conducted by optimizing the size of Pure Al powders, different powder material additive and applied pressure parameters. Besides, further studies can be conducted to find other optimum conditions by changing other parameters, such as induction coil design, the frequency and the applied power of the induction system [11,17,21,22]. The induction technique can provide better information about the change in the material surface's internal structure and possible hardness increase. The hardness change is proof of surface hardening by heat treatment which is carried out during induction sintering.

#### 4. RESULTS VE DISCUSSION

In this study, 30 Bar pressure was applied to 15 µm Pure Al powders under cold press, and sintering was provided by furnace and induction. Obtained results are presented below.

- In all induction sintered samples, the density after sintering increased compared to the raw density. As a result, the porosity decreased. In addition, as the temperature increases in these samples, the percentage change in density decreases.
- It is found out that using the induction sintering method is more advantageous to obtain a better hardness when different sintering methods are compared.
- Hardness decreased as the sintering temperature increased in all samples. On the other hand, the best hardness value was obtained after 5 minutes of induction and sintering at the specified temperatures.
- An increase in density was detected in sample 10, sintered with a furnace at 600°C. On the other hand, a decrease in density was observed in samples 11 and 12 sintered with a furnace close to and above the melting temperature of aluminum (650°C and 700°C). The melting of the material above the sintering temperature causes a decrease in density.
- Porosity decreased in induction-sintered samples. The decrease in the material's porous structure caused its size to decrease and its density to increase. Accordingly, the hardness values of the material increased.
- Induction-sintered samples are sintered faster than furnace-sintered samples. In this context, it is possible to save time with the induction sintering method.

#### 6. CONFLICTS OF INTEREST

The authors declare no conflict of interest.

#### 7. REFERENCES

1. Gökçe, A., Fındık, F., & Kurt, A. O. (2017). Alüminyum ve alaşımlarının toz metalurjisi işlemleri. *Mühendis ve Makina*, 58(686), 21-47.
2. Halil, A. R. I. K., Kırmızı, G., & Semerci, P. (2017). Sıcak presleme ile alüminyum matrisli ve al<sub>2</sub>O<sub>3</sub> takviyeli toz metal kompozit malzeme üretimi ve abrasif aşınma davranışının araştırılması. *Gazi University Journal of Science Part C: Design and Technology*, 5(4), 87-97.
3. Kumar, N., Bharti, A., & Saxena, K. K. (2021). A re-investigation: Effect of powder metallurgy parameters on the physical and mechanical properties of aluminium matrix composites. *Materials Today: Proceedings*, 44, 2188-2193.



4. Pickens, J. R. (1981). Aluminium powder metallurgy technology for high-strength applications. *Journal of Materials Science*, 16, 1437-1457.
5. Nassar, A. E., & Nassar, E. E. (2017). Properties of aluminum matrix Nano composites prepared by powder metallurgy processing. *Journal of King Saud University-Engineering Sciences*, 29(3), 295-299.
6. Anderson, I. E., & Foley, J. C. (2001). Determining the role of surfaces and interfaces in the powder metallurgy processing of aluminum alloy powders. *Surface and Interface Analysis*, 31(7), 599-608.
7. Awotunde, M. A., Adegbenjo, A. O., Shongwe, M. B., & Olubambi, P. A. (2019). Spark Plasma Sintering of Aluminium-Based Materials. In *Spark Plasma Sintering of Materials*, Spring eBooks, 191–218. [https://doi.org/10.1007/978-3-030-05327-7\\_7](https://doi.org/10.1007/978-3-030-05327-7_7)
8. Hsieh, C. T., Ho, Y. C., Wang, H., Sugiyama, S., & Yanagimoto, J. (2020). Mechanical and tribological characterization of nanostructured graphene sheets/A6061 composites fabricated by induction sintering and hot extrusion. *Materials Science and Engineering: A*, 786, 138998.
9. Seikh, A. H., Baig, M., Singh, J. K., Mohammed, J. A., Luqman, M., Abdo, H. S., ... & Alharthi, N. H. (2019). Microstructural and corrosion characteristics of Al-Fe alloys produced by high-frequency induction-sintering process. *Coatings*, 9(10), 686.
10. Mendoza, J. M., Estrada-Guel, I., Garay, C., Romero, M. I., Perez-Bustamante, R., Carreño-Gallardo, C., & Martínez-Sánchez, R. Impact of process conditions on the mechanical properties, structure and microstructure of milled aluminum sintered through rapid induction heating. SSRN, [https://papers.ssrn.com/sol3/papers.cfm?abstract\\_id=4273156](https://papers.ssrn.com/sol3/papers.cfm?abstract_id=4273156)
11. Ujah, C. O., & Kallon, D. V. V. (2022). Trends in aluminium matrix composite development. *Crystals*, 12(10), 1357.
12. Dudina, D. V., Georgarakis, K., & Olevsky, E. A. (2023). Progress in aluminium and magnesium matrix composites obtained by spark plasma, microwave and induction sintering. *International Materials Reviews*, 68(2), 225-246.
13. Oliver, U. C., Sunday, A. V., Christain, E. I. E. I., & Elizabeth, M. M. (2021). Spark plasma sintering of aluminium composites—a review. *The International Journal of Advanced Manufacturing Technology*, 112, 1819-1839.
14. Çavdar, U., & Sarı Çavdar, P. (2019). Demir esaslı toz metal malzemelerin ultra-yüksek frekanslı indüksiyon sistemi ile sinterleme sıcaklığı optimizasyonu, *Niğde Ömer Halisdemir Üniversitesi Mühendislik Bilimleri Dergisi*, 8(2009), 378-383.
15. Choudhury, A., Nanda, J., & Das, S. N. (2021, November). Sintering sensitivity of aluminium metal matrix composites developed through powder metallurgy proposed technique-a review. *Journal of Physics: Conference Series*, 2070(1), 012193. IOP Publishing.
16. Akkurt, O., Altıntaş, A., Çavdar, P., & Çavdar, U. Effect on the mechanical properties of sintering process of aluminium alloys. *International Scientific and Vocational Studies Journal*, 3(2), 85-91.
17. Taştan, M., Gökozan, H., Çavdar, P. S., Soy, G., & Çavdar, U. (2020). Cost analysis of T6 induction heat treatment for the aluminum-copper powder metal compacts. *Science of Sintering*, 52(1), 77-85.
18. Kohli, A., & Singh, H. (2011). Optimization of processing parameters in induction hardening using response surface methodology. *Sadhana*, 36(2), 141-152.
19. Palaniradja, K., Alagumurthi, N., & Soundararajan, V. (2010). Modeling of phase transformation in induction hardening. *The Open Materials Science Journal*, 4(1), 64-73

**20.** Çavdar, U., Taştan, M., Gökozan, H., Soy, G., & Çavdar, P. S. (2021). Heat treatment of 2024 and 5083 aluminum materials by induction, a competitive method, and cost analysis. *Journal of Inorganic and Organometallic Polymers and Materials*, 31, 1754-1763.

**21.** Çubuk, H. S., & Çavdar, U. Investigation of mechanical properties of nano boron nitride added aluminum material produced by different production method. *International Scientific and Vocational Studies Journal*, 6(2), 51-59.

**22.** Karaca, B., & Çavdar, U. (2014). Saf ve bor karbür takviyeli alüminyum tozlarının ultra yüksek frekanslı indüksiyon jeneratörü ile sinterlenmesi. *Mühendis ve Makina*, 55(657), 59-64.

<b>IDUNAS</b>	<b>NATURAL &amp; APPLIED SCIENCES JOURNAL</b>	2023 Vol. 6 No. 1 (41-49)
---------------	---	------------------------------------

## Relations of Multiplicative Generalized $(\alpha, \beta)$ – Reverse Derivation and $\alpha$ – Commuting Maps

Research Article

Barış ALBAYRAK <sup>1\*</sup> 

<sup>1</sup>Department of Finance and Banking, Çanakkale Onsekiz Mart University, Turkey.

Author E-mails  
balbayrak@comu.edu.tr

\*Correspondence to: Barış ALBAYRAK, Department of Finance and Banking, Çanakkale Onsekiz Mart University, Turkey.

DOI: 10.38061/idunas.1260138

Received: 04.03.2023; Accepted: 03.07.2023

### Abstract

In this paper, properties of the ideal  $I$  of semiprime ring  $R$  with multiplicative generalized  $(\alpha, \beta)$  – reverse derivation with determined not necessarily additive map  $d$  is studied. We generalized previous studies for different derivations to multiplicative generalized  $(\alpha, \beta)$  – reverse derivation  $F$ . We show that  $[\beta(p), d(p)]I = 0$  for all  $p \in I$  or  $[d(p)], \alpha(p)]I = 0$  for all  $p \in I$  under the given different conditions. Also, we give the relationship between map  $d$  and anti-automorphism  $\alpha$  of semiprime ring  $R$  and automorphism  $\beta$  of semiprime ring  $R$ . Under the given different conditions, we examine whether  $d$  is  $\alpha$  – commuting on ideal  $I$  or  $\beta$  – commuting on ideal  $I$  and obtain new results.

**Keywords:** Reverse derivation, semiprime ring, commuting map

2010 Mathematics Subject Classification. Primary 16N60; Secondary 16U80, 16W25.

### 1. INTRODUCTION

The aim of our study is to investigate properties of the ideal  $I$  of semiprime ring  $R$  with multiplicative generalized  $(\alpha, \beta)$  –reverse derivation. How to generalize the work on semiprime rings involving derivation and how to obtain new results has been a long-studied topic in ring theory. The definition of derivation is given as additive map  $d$  that provides  $d(rp) = d(r)p + rd(p)$  for  $r, p \in R$ . This definition has been generalized over time and studies have been generalized for different derivations. In order to contribute to these studies, we study multiplicative generalized  $(\alpha, \beta)$  –reverse derivation and we obtain

new results. Before moving on to the main conclusions, let's give some previous studies and terms that we will use throughout this article.

Let  $Z(R)$  denote the center of ring  $R$ . Assume that  $pRp = (0)$  for any  $p \in R$ .  $R$  is said to be a semiprime ring, if  $p = 0$ .  $[p, r]$  expression is used for commutator  $pr - rp$  and  $(por)$  expression is used for anticommutator  $pr + rp$ . A subgroup  $I$  which is additive is said to be an ideal of  $R$  if  $IR$  and  $RI$  are included  $I$ .

The generalized derivation definition was first given by Bresar in [1].  $F$  from  $R$  to  $R$  is said to be generalized derivation with determined derivation  $d$  if  $F(rp) = F(r)p + rd(p)$  for  $r, p \in R$ . According to [2], generalized derivation  $F$  is called generalized  $\alpha$ -derivation with determined derivation  $d$  if  $F(rp) = F(r)\alpha(p) + \alpha(r)d(p)$  for  $r, p \in R$ . On the other hand, Herstein introduced reverse derivation in [3]. If an additive map  $d$  provides  $d(rp) = d(p)r + pd(r)$  for any  $r, p \in R$ , then  $d$  is a reverse derivation.

Later on, derivations with non-additive maps began to be studied. In [4,5,6], authors gave different definitions of the derivation when  $d$  is a non-additive map (not necessarily additive). A non-additive map  $d$  is said to be multiplicative derivation if it provides  $d(rp) = d(r)p + rd(p)$  for  $r, p \in R$ .  $F$  from  $R$  in  $R$  is said to be multiplicative generalized derivation with determined non-additive map (not necessarily additive)  $d$  if  $F(rp) = F(r)p + rd(p)$  for  $r, p \in R$ .

Next, in [7], authors gave the definitions of multiplicative generalized reverse derivation and multiplicative generalized  $(\alpha, \beta)$ -reverse derivation.  $F$  is said to be multiplicative generalized reverse derivation with determined a non-additive map (not necessarily additive)  $d$  if  $F(rp) = F(p)r + pd(r)$ .  $F$  is said to be multiplicative generalized  $(\alpha, \beta)$ -reverse derivation with determined a non-additive map (not necessarily additive)  $d$  if  $F(rp) = F(p)\alpha(r) + \beta(p)d(r)$  for an automorphism  $\beta$  of  $R$  and anti-automorphism  $\alpha$  of  $R$ .

On the other hand, different types of maps used in derivation studies were also defined. A map  $d$  from  $R$  to  $R$  that provides  $[d(p), p] = 0$  for all  $p \in R$ , is said to be commuting on  $R$ . Also, for  $\alpha$  automorphism of  $R$ , a map  $d$  from  $R$  to  $R$  that provides  $[d(p), \alpha(p)] = 0$  for all  $p \in R$ , is said to be  $\alpha$ -commuting on  $R$ . Similar definitions can be made for anti-automorphism. Authors introduced multiplicative left reverse  $\alpha$ -centralizer in [8]. A map  $d$  from  $R$  to  $R$  is called a multiplicative left reverse  $\alpha$ -centralizer satisfy  $d(pr) = d(r)\alpha(p)$  holds for all  $p, r \in R$ .  $\alpha$  is a mapping of  $R$  and  $d$  is a map such that not necessarily additive.

Let's take a brief look at the work we have done in this study. In [9] authors studied identities  $F(por) + H(por) = 0$ ,  $F(por) + H[p, r] = 0$ ,  $F[p, r] + [\alpha(p), H(r)] = 0$ ,  $F(por) + [\alpha(p), H(r)] = 0$ ,  $F(rp) + [\alpha(p), H(r)] \in Z(R)$ ,  $F(rp) + [H(p), H(r)] \in Z(R)$  for all  $r, p \in I$  such that  $F$  is a multiplicative generalized derivation,  $I$  is an ideal semiprime ring  $R$ . We generalize their results to multiplicative generalized  $(\alpha, \beta)$ -reverse derivation  $F$  for anti-automorphism  $\alpha$  and automorphism  $\beta$  of semiprime ring  $R$ . Also, we examine the relationship between multiplicative generalized  $(\alpha, \beta)$ -reverse derivations and  $\alpha$ -commuting maps.

## 2. PRELIMINARIES

Let's first give the properties provided for the anticommutator and commutator for all  $s, r, p \in R$ . Next, we will give a lemma that we will use in our theorems.

- $[pr, s] = p[r, s] + [p, s]r$
- $[p, rs] = [p, r]s + r[p, s]$
- $(pr)os = p(ros) - [p, s]r = (pos)r + p[r, s]$
- $p \circ (rs) = (por)s - r[p, s] = r(pos) + [p, r]s$

**Lemma 2.1** [10] *Let  $R$  be a 2-torsion free semiprime ring and  $U$  a noncentral Lie ideal of  $R$ . If  $pU = 0$  for  $p \in U$ , then  $p = 0$ .*

**3. RESULTS**

Let  $R$  be a semiprime ring,  $0 \neq I$  be an ideal of  $R$ ,  $\alpha$  be an anti-automorphism of  $R$ ,  $\beta$  be an automorphism of  $R$ ,  $0 \neq G: R \rightarrow R$  be a multiplicative left reverse  $\alpha$ -centralizer and  $0 \neq F: R \rightarrow R$  be a multiplicative generalized  $(\alpha, \beta)$ -reverse derivation determined with a map  $0 \neq d: R \rightarrow R$  such that it doesn't need to be an additive map. In the following theorems, we examine the conditions under which  $[\beta(p), d(p)]I = 0$  is provided for all  $p \in I$ .

**Theorem 3.1:** *If  $F(por) + G(por) = 0$  for all  $r, p \in I$ , then  $[\beta(p), d(p)]I = 0$  for all  $p \in I$ .*

**Proof:** Let  $F(por) + G(por) = 0$  for all  $r, p \in I$ . Replacing  $r$  by  $pr$  and using commutator properties, we have

$$\begin{aligned} 0 &= F(po(pr)) + G(po(pr)) \\ &= F(p(por)) + G(p(por)) \end{aligned}$$

for all  $r, p \in I$ . Using commutator properties and definitions of  $F$  and  $G$ , we get

$$F(por)\alpha(p) + \beta(por)d(p) + G(por)\alpha(p) = 0$$

for all  $r, p \in I$ . Using hypothesis, we have

$$\beta(por)d(p) = 0 \text{ for all } r, p \in I. \tag{1}$$

Replacing  $r$  by  $\beta^{-1}(r)s$ ,  $s \in I$  and using commutator properties, we have

$$r\beta(pos)d(p) + \beta[p, \beta^{-1}(r)]\beta(s)d(p) = 0$$

for all  $s, r, p \in I$ . Using equation (1) in the above equation, we obtain

$$\beta[p, \beta^{-1}(r)]\beta(s)d(p) = 0 \text{ for all } s, r, p \in I.$$

Since  $\beta$  is an automorphism of  $R$ , we write this relation as below relation.

$$[\beta(p), r]Vd(p) = 0 \text{ for all } r, p \in I.$$

where  $\beta(I) = V$  is a nonzero ideal of  $R$ . Replacing  $r$  by  $d(p)r$ , we have

$$[\beta(p), d(p)]rwd(p) = 0 \text{ for all } r, p \in I, w \in V. \tag{2}$$

Replacing  $w$  by  $w\beta(p)$ , we have

$$[\beta(p), d(p)]rw\beta(p)d(p) = 0 \tag{3}$$

for all  $r, p \in I, w \in V$ . Also, right multiplication of equation (2) by  $\beta(p)$ , we get

$$[\beta(p), d(p)]rwd(p)\beta(p) = 0 \tag{4}$$

for all  $r, p \in I, w \in V$ . Comparing (3) and (4), we get

$$[\beta(p), d(p)]IV[\beta(p), d(p)] = 0 \text{ for all } p \in I.$$

Since  $V$  is an ideal of  $R$ , we write

$$[\beta(p), d(p)]IVR[\beta(p), d(p)]IV = 0 \text{ for all } p \in I.$$

Since  $R$  is a semiprime ring, we obtain

$$[\beta(p), d(p)]IV = 0 \text{ for all } p \in I.$$

Specially, we write

$$[\beta(p), d(p)]I\beta(s) = 0 \text{ for all } s, p \in I. \tag{5}$$

Replacing  $s$  by  $s\beta^{-1}(d(p))$ , we have

$$[\beta(p), d(p)]I\beta(s)d(p) = 0 \tag{6}$$

for all  $s, p \in I$ . Also, since  $I$  is an ideal of  $R$ , from equation (5) we write

$$[\beta(p), d(p)]Id(p)\beta(s) = 0 \tag{7}$$

**Theorem 3.2:** If  $F(por) + G[p, r] = 0$  for all  $r, p \in I$ , then  $[\beta(p), d(p)]I = 0$  for all  $p \in I$ .

**Proof:** Let  $F(por) + G[p, r] = 0$  for all  $r, p \in I$ . Replacing  $r$  by  $pr$  and using commutator properties, we have

$$0 = F(po(pr)) + G[p, pr] = F(p(por)) + G(p[p, r])$$

for all  $r, p \in I$ . Using commutator properties and definitions of  $F$  and  $G$ , we get

$$F(por)\alpha(p) + \beta(por)d(p) + G(por)\alpha(p) = 0$$

for all  $r, p \in I$ . Using hypothesis, we have

$$\beta(por)d(p) = 0 \text{ for all } r, p \in I.$$

This equation is the equation (1) in Theorem 3.1. If the proof is continued in a similar way,

$$[\beta(p), d(p)]I = 0$$

is obtained.

**Theorem 3.3:** If  $F[p, r] + [\alpha(p), G(r)] = 0$  for all  $r, p \in I$ , then  $[\beta(p), d(p)]I = 0$  for all  $p \in I$ .

**Proof:** Let  $F[p, r] + [\alpha(p), G(r)] = 0$  for all  $r, p \in I$ . Replacing  $r$  by  $pr$  and using commutator properties, we have

$$F[p, pr] + [\alpha(p), G(pr)] = F[p[p, r]] + [\alpha(p), G(pr)] = 0$$

for all  $r, p \in I$ . Using commutator properties and definitions of  $F$  and  $G$ , we get

$$F[p, r]\alpha(p) + \beta[p, r]d(p) + [\alpha(p), G(r)]\alpha(p) + G(r)[\alpha(p), \alpha(p)] = 0 \text{ for all } r, p \in I$$

Using hypothesis, we have

$$\beta[p, r]d(p) = 0 \text{ for all } r, p \in I. \tag{8}$$

Replacing  $r$  by  $\beta^{-1}(r)s$ ,  $s \in I$  and using commutator properties, we have

$$\beta[p, \beta^{-1}(r)]\beta(s)d(p) + r\beta[p, s]d(p) = 0$$

for all  $s, r, p \in I$ . Using equation (8) in the above equation, we obtain

$$\beta [p, \beta^{-1}(r)] \beta(s)d(p) = 0 \text{ for all } s, r, p \in I.$$

Since  $\beta$  is an automorphism of  $R$ , we write this relation as below relation.

$$[\beta(p), r]Vd(p) = 0 \text{ for all } r, p \in I.$$

where  $\beta(I) = V$  is a nonzero ideal of  $R$ . Replacing  $r$  by  $d(p)r$ , we have

$$[\beta(p), d(p)]rwd(p) = 0 \text{ for all } r, p \in I, w \in V.$$

This equation is the equation (2) in Theorem 3.1. If the proof is continued in a similar way,

$$[\beta(p), d(p)]I = 0$$

is obtained.

**Theorem 3.4:** If  $F(por) + [\alpha(p), G(r)] = 0$  for all  $r, p \in I$ , then  $[\beta(p), d(p)]I = 0$  for all  $p \in I$ .

**Proof:** Let  $F(por) + [\alpha(p), G(r)] = 0$  for all  $r, p \in I$ . Replacing  $r$  by  $pr$  and using commutator properties, we have

$$F(po(pr)) + [\alpha(p), G(pr)] = F(p(por)) + [\alpha(p), G(pr)] = 0$$

for all  $r, p \in I$ . Using commutator properties and definitions of  $F$  and  $G$ , we get

$$F(por)\alpha(p) + \beta(por)d(p) + [\alpha(p), G(r)]\alpha(p) + G(r)[\alpha(p), \alpha(p)] = 0 \text{ for all } r, p \in I.$$

Using hypothesis, we have

$$\beta(por)d(p) = 0 \text{ for all } r, p \in I.$$

This equation is the equation (1) in Theorem 3.1. If the proof is continued in a similar way,

$$[\beta(p), d(p)]I = 0$$

is obtained.

Now, using the Lemma 2.1, we can obtain the following result.

**Corollary 3.5:** Let  $R$  be a 2-torsion free semiprime ring,  $I \not\subseteq Z(R)$  be an ideal of  $R$ ,  $\alpha$  be an anti-automorphism of  $R$ ,  $\beta$  be an automorphism of  $R$ ,  $0 \neq G: R \rightarrow R$  be a multiplicative left reverse  $\alpha$  – centralizer and  $0 \neq F: R \rightarrow R$  be a multiplicative generalized  $(\alpha, \beta)$  – reverse derivation determined with a map  $0 \neq d: R \rightarrow R$  such that it doesn't need to be an additive map. If one of the following properties are provided for all  $r, p \in I$ , then  $d$  is  $\beta$  – commuting on  $I$ .

- 1)  $F(por) + G(por) = 0$
- 2)  $F(por) + G[p, r] = 0$
- 3)  $F[p, r] + [\alpha(p), G(r)] = 0$
- 4)  $F(por) + [\alpha(p), G(r)] = 0$

Now, let's give the relationship between map  $d$  and anti-automorphism  $\alpha$ .

**Theorem 3.6:** If  $\beta(pr) = \alpha(rp)$  and  $F(rp) + [\alpha(p), G(r)] \in Z(R)$  for all  $r, p \in I$ , then  $[d(p), \alpha(p)]I = 0$  for all  $p \in I$ .

**Proof:** Let  $F(rp) + [\alpha(p), G(r)] \in Z(R)$  for all  $r, p \in I$ . Replacing  $r$  by  $vr$ ,  $v \in I$  and using commutator properties, we have

$$F(vrp) + [\alpha(p), G(vr)] \in Z(R) \tag{9}$$

for all  $v, r, p \in I$ . Using commutator properties and definitions of  $F$  and  $G$ , we get

$$(F(rp) + [\alpha(p), G(r)])\alpha(v) + \beta(rp)d(v) + G(r)[\alpha(p), \alpha(v)] \in Z(R)$$

for all  $v, r, p \in I$ . Since the element in the above equation is in the  $Z(R)$ , we write following equation for  $\alpha(v)$ .

$$[(F(rp) + [\alpha(p), G(r)])\alpha(v) + \beta(rp)d(v) + G(r)[\alpha(p), \alpha(v)], \alpha(v)] = 0$$

for all  $v, r, p \in I$ . Using hypothesis, we have

$$[\beta(rp)d(v), \alpha(v)] + [G(r)[\alpha(p), \alpha(v)], \alpha(v)] = 0$$

for all  $v, r, p \in I$ . Using the fact that  $\beta(pr) = \alpha(rp)$  for all  $r, p \in I$ , we obtain

$$[\alpha(pr)d(v), \alpha(v)] + [G(r)[\alpha(p), \alpha(v)], \alpha(v)] = 0 \tag{10}$$

for all  $v, r, p \in I$ . Replacing  $p$  by  $vp$  and using commutator properties, we have

$$[\alpha(vpr)d(v), \alpha(v)] + [G(r)[\alpha(p), \alpha(v)]\alpha(v), \alpha(v)] = 0 \tag{11}$$

for all  $v, r, p \in I$ . Also, right multiplication of equation (10) by  $\alpha(v)$ , we get

$$[\alpha(pr)d(v) \alpha(v), \alpha(v)] + [G(r)[\alpha(p), \alpha(v)] \alpha(v), \alpha(v)] = 0 \tag{12}$$

for all  $v, r, p \in I$ . Comparing (11) and (12) and using properties of anti-automorphism for  $\alpha$ , we get

$$[\alpha(r)\alpha(p)d(v) \alpha(v), \alpha(v)] - [\alpha(r)\alpha(p)\alpha(v)d(v), \alpha(v)] = 0 \text{ for all } v, r, p \in I.$$

Arranging above equation, we have

$$[\alpha(r)\alpha(p)[d(v), \alpha(v)], \alpha(v)] = 0 \tag{13}$$

for all  $v, r, p \in I$ . Replacing  $r$  by  $rw$ ,  $w \in I$ , we have

$$[\alpha(w)\alpha(r)\alpha(p)[d(v), \alpha(v)], \alpha(v)] = 0$$

for all  $w, v, r, p \in I$ . Using commutator properties, we get

$$\alpha(w)[\alpha(r)\alpha(p)[d(v), \alpha(v)], \alpha(v)] + [\alpha(w), \alpha(v)]\alpha(r)\alpha(p)[d(v), \alpha(v)] = 0$$

for all  $w, v, r, p \in I$ . Using equation (13) in the above equation, we obtain

$$[\alpha(w), \alpha(v)]\alpha(r)\alpha(p)[d(v), \alpha(v)] = 0$$

for all  $w, v, r, p \in I$ . Since  $\alpha$  is an anti-automorphism of  $R$ , we write this relation as below relation.

$$[\alpha(w), \alpha(v)]VV[d(v), \alpha(v)] = 0 \text{ for all } w, v \in I.$$

where  $\alpha(I) = V$  is a nonzero ideal of  $R$ . Replacing  $w$  by  $v$ , we have

$$[\alpha(v), \alpha(v)]VV[d(v), \alpha(v)] = 0 \text{ for all } v \in I.$$

Since  $V$  is an ideal of  $R$ , left and right multiplication of above equation by  $V$ , we get

$$V[\alpha(v), \alpha(v)]VRV[d(v), \alpha(v)]V = 0 \text{ for all } v \in I.$$

Since  $R$  is a semiprime ring, we get



$$V[d(v), \alpha(v)]V = 0 \text{ for all } v \in I.$$

Using properties of ideal  $V$ , we have

$$[d(v), \alpha(v)]VR[d(v), \alpha(v)]V = 0 \text{ for all } v \in I.$$

Using the fact that  $R$  is a semiprime ring, we obtain

$$[d(v), \alpha(v)]V = 0 \text{ for all } v \in I.$$

Since  $V$  is an ideal of  $R$ , we get

$$[d(v), \alpha(v)]IV = 0 \text{ for all } v \in I.$$

Specially, we write

$$[d(v), \alpha(v)]I\alpha(s) = 0 \text{ for all } s, v \in I \tag{14}$$

Replacing  $s$  by  $s\alpha^{-1}(d(v))$ , we have

$$[d(v), \alpha(v)]I\alpha(s)d(v) = 0 \tag{15}$$

for all  $s, v \in I$ . Also, since  $I$  is an ideal of  $R$ , from equation (14), we write

$$[d(v), \alpha(v)]Id(v)\alpha(s) = 0 \tag{16}$$

for all  $s, v \in I$ . Comparing (15) and (16), we get

$$[d(v), \alpha(v)]I[d(v), \alpha(s)] = 0 \text{ for all } s, v \in I.$$

Replacing  $s$  by  $v$  we have

$$[d(v), \alpha(v)]I[d(v), \alpha(v)] = 0 \text{ for all } v \in I.$$

Since  $I$  is an ideal of  $R$ , we write

$$[d(v), \alpha(v)]IR[d(v), \alpha(v)]I = 0 \text{ for all } v \in I$$

Since  $R$  is a semiprime ring, we obtain

$$[d(v), \alpha(v)]I = 0 \text{ for all } v \in I.$$

**Theorem 3.7:** If  $\beta(rp) = \alpha(rp)$  and  $F(rp) + [G(p), G(r)] \in Z(R)$  for all  $r, p \in I$ , then  $[d(p), \alpha(p)]I = 0$  for all  $p \in I$ .

**Proof:** Let  $F(rp) + [G(p), G(r)] \in Z(R)$  for all  $r, p \in I$ . Replacing  $r$  by  $vr$ ,  $v \in I$  and using commutator properties, we have

$$F(vrp) + [G(p), G(vr)] \in Z(R)$$

for all  $v, r, p \in I$ . Using commutator properties and definitions of  $F$  and  $G$ , we get

$$(F(rp) + [G(p), G(r)])\alpha(v) + \beta(rp)d(v) + G(r)[\alpha(p), \alpha(v)] \in Z(R)$$

for all  $v, r, p \in I$ . Since the element in the above equation is in the  $Z(R)$ , we write following equation for  $\alpha(v)$ .

$$[(F(rp) + [G(p), G(r)])\alpha(v) + \beta(rp)d(v) + G(r)[\alpha(p), \alpha(v)], \alpha(v)] = 0$$

for all  $v, r, p \in I$ . Using hypothesis in this relation, we have

$$[\beta(rp)d(v), \alpha(v)] + [G(r)[\alpha(p), \alpha(v)], \alpha(v)] = 0$$

for all  $v, r, p \in I$ . Using the fact that  $\beta(pr) = \alpha(rp)$  for all  $r, p \in I$ , we obtain

$$[\alpha(pr)d(v), \alpha(v)] + [G(r)[\alpha(p), \alpha(v)], \alpha(v)] = 0$$

for all  $v, r, p \in I$ . This equation is the equation (10) in Theorem 3.6. If the proof is continued in a similar way,

$$[d(p), \alpha(p)]I = 0$$

is obtained.

Now, using the Lemma 2.1, we can obtain the following result.

**Corollary 3.8:** Let  $R$  be a 2-torsion free semiprime ring,  $I \not\subseteq Z(R)$  be an ideal of  $R$ ,  $\alpha$  be an anti-automorphism of  $R$ ,  $\beta$  be an automorphism of  $R$  such that  $\beta(pr) = \alpha(rp)$  for all  $r, p \in I$ ,  $0 \neq G: R \rightarrow R$  be a multiplicative left reverse  $\alpha -$  centralizer and  $0 \neq F: R \rightarrow R$  be a multiplicative generalized  $(\alpha, \beta) -$  reverse derivation determined with a map  $0 \neq d: R \rightarrow R$  such that it doesn't need to be an additive map. If one of the following properties are provided for all  $r, p \in I$ , then  $d$  is  $\alpha -$  commuting on  $I$ .

- 1)  $F(rp) + [\alpha(p), G(r)] \in Z(R)$
- 2)  $F(rp) + [G(p), G(r)] \in Z(R)$

## 5. CONCLUSIONS

In this paper, properties of the ideal  $I$  of semiprime ring  $R$  with multiplicative generalized  $(\alpha, \beta) -$  reverse derivation with determined not necessarily additive map  $d$  is studied. Many studies have been done on the derivation and commutativity in the prime ring and the results have been reached. These studies and reached results is adapted for multiplicative generalized  $(\alpha, \beta) -$  reverse derivation  $F$  in our study. Also, new results are given about the relationship between map  $d$  and anti-automorphism  $\alpha$ . The studies and the results found can be used for different derivations and semiprime rings in the future and contribute to the ring theory.

## 6. REFERENCES

- [1] Bresar, M. (1991). On the distance of the composition of two derivations to the generalized derivations. *Glaskow Math. J.*, 33,89-93.
- [2] Chang, J. C. (2009). Right generalized  $(\alpha, \beta) -$  derivations having power central values. *Taiwanese J. Math.*, 13(4), 1111-1120.
- [3] Herstein, I. N. (1957). Jordan Derivation of Prime Rings. *Proc. Amer. Math. Soc.* 8, 1104-1110.
- [4] Dhara, B. and Ali, S. (2013). On Multiplicative (generalized) derivative in prime and semi-prime rings”, *Aequat. Math.*, 86(1-2), 65-79.
- [5] Daif, M.N. (1991) When is a multiplicative derivation additive. *Int. J. Math. Sci.*, 14(3), 615-618.
- [6] Daif, M.N. and Tammam El Sayiad M.S. (2007). Multiplicative generalized Derivation which are additive. *East-west J. Math.* 9(1), 31-37.

- [7] Tiwari, S.K., Sharma, R.K. and Dhara, B. (2008). Some theorems of commutativity on semiprime ring with mapping. *Southeast Asian Bull. Math.*, 42(2), 279-292
- [8] Alhaidary, Z. S. M. and Majeed, A. H. (2021). Square closed Lie Ideals and Multiplicative (Generalized)  $(\alpha, \beta)$  –reverse derivation of Prime Rings. *Journal of Discrete Math. Sci. and Cryptography*, 24(7), 2037-2046.
- [9] Malleswari, G. N., Sreenivasulu, S. and Shobhalatha. G. (2021). Semiprime rings with multiplicative (Generalized) – derivations involving left multipliers. *Create. Math. Inform*, 30(1), 61-68.
- [10] Hongan, M., Rehman, N. and Al-Omary R. M. (2011). Lie ideals and Jordan triple derivations in rings. *Rend. Sem. Mat. Univ. Padova*, 125.